Patterned apoptosis has an instructive role for local growth and tissue shape regulation in a fast-growing epithelium

Alexis Matamoro-Vidal, Tom Cumming, Anđela Davidović, Florence Levillayer, Romain Levayer

Patterned apoptosis has an instructive role for local growth and tissue shape regulation in a fast-growing epithelium

Alexis Matamoro-Vidal[1], Tom Cumming[1,2], Anđela Davidović[3], Florence Levillayer[1] and Romain Levayer[1*§]

1. Department of Developmental and Stem Cell Biology, Institut Pasteur, CNRS UMR 3738, Université Paris Cité, Cell Death and Epithelial Homeostasis Unit, F-75015 Paris, France

2. PPU program Institut Pasteur, Sorbonne Université, Collège Doctoral, F75005 Paris, France

3. Institut Pasteur, Université Paris Cité, Bioinformatics and Biostatistics Hub, F-75015 Paris, France

* Correspondance to: romain.levayer@pasteur.fr

§ Lead contact

Abstract

What regulates organ size and shape remains one of the fundamental mysteries of modern biology. Research in this area has primarily focused on deciphering the regulation in time and space of growth and cell division, while the contribution of cell death has been much more neglected. This includes studies of the *Drosophila* wing, which represents one of the best characterised systems for the study of growth and patterning, and undergoes massive growth during larval stage and important morphogenetic remodeling during pupal stage. So far, it has been assumed that cell death was relatively neglectable in this tissue both during larval and pupal stage and as a result the pattern of growth was usually attributed to the distribution of cell division. Here, using systematic mapping and registration combined with quantitative assessment of clone size and disappearance as well as live imaging, we outline a persistent pattern of cell death and clone elimination emerging in the larval wing disc and persisting during pupal wing morphogenesis. Local variation of cell death is associated with local variation of clone size, pointing to an impact of cell death on local growth which is not fully compensated by proliferation. Using morphometric

analyses of adult wing shape and genetic perturbations, we provide evidence that patterned death affects locally and globally adult wing shape and size. This study describes a roadmap for precise assessment of the contribution of cell death to tissue shape, and outlines an important instructive role of cell death in modulating quantitatively local growth and morphogenesis of a fast-growing tissue.

Keywords: apoptosis, morphogenesis, growth, clone dynamics, quantitative mapping, *Drosophila*, wing imaginal disc

Introduction

The search of cellular mechanisms underlying variation in organ's size and shape is essential to our understanding of health and evolution. These mechanisms include changes in cell shape, cell proliferation, oriented cell division, oriented cell intercalation and also cell death [1]. Programmed cell death and apoptosis are indeed essential regulators of development and morphogenesis [2]. For instance, cell death is required to eliminate scaffolding tissues which are not present in the adult body. Apoptosis in epithelia is also a driving force of morphogenesis which can help to fuse tissues by generating pulling forces [3] or trigger fold formations by generating apico-basal traction forces [4, 5]. Finally, apoptosis has been associated with the buffering of developmental fluctuations which can eliminate miss-specified/miss-patterned cells through cell competition [6], morphogenetic apoptosis [7, 8], cell sorting and extrusion [9-11] or more recently, with the buffering of mismatch between the size of the tissue and the shape of morphogen gradients [12]. Interestingly, while the functions of apoptosis are numerous, its contribution to the regulation of organ size and growth, especially in tissues undergoing fast expansion, has been poorly studied. Accordingly, emphasis has mostly been given to cellular growth regulation including the increase of cell volume and cell proliferation [13-21]. Moreover, systematic and quantitative evaluations of the pattern and number of cell deaths remain relatively rare and tedious, especially in tissues which are not appropriate for long term live imaging [22-24]. As such, the exact pattern of cell death and its real contribution to the regulation of organ size and shape remain poorly documented in many situations. This also applies to the *Drosophila* wing, one of the best studied systems for understanding patterning and growth regulation [15, 17, 25-28].

Drosophila wing development can be separated in the larval stage, where the wing imaginal disc mostly undergoes massive proliferation and patterning, followed by the pupal stage, where complex morphogenetic movements give rise to the final wing shape [29]. At larval stages, *Drosophila* wing imaginal discs are epithelial sacs composed of two epithelia: the peripodial cells (squamous epithelium) and a pseudostratified epithelium that will form the adult structures [30]. The disc is separated into a distal domain that will give rise to the adult wing blade (the wing pouch, or wing proper) and a proximal region called the hinge which will connect the wing to the thorax. This wing pouch is patterned in different domains prefiguring adult wing structures: the pro-vein domains L2 to L5 and the dorsal-ventral boundary that will give rise respectively to the adult wing veins and the adult wing boundaries (**Figure 1A,B**). Wing imaginal discs undergo massive growth during larval development through several rounds of cell division (9 to 11 cycles) [31, 32]. This growth phase is followed by profound remodeling and morphogenesis during the pupal stage [33] including wing eversion and apposition of the dorsal and ventral epithelial layers [34, 35], the elongation of the wing proper through distal anchoring and hinge contraction [27, 36], global tissue growth by cell expansion and folding [37] eventually followed by hatching and wing spreading[38] (**Figure 1A,B**). All these steps are performed with a high degree of precision and reproducibility leading to extremely reproducible shape, specially comparing left and right wings [39].

Decades of work sought to dissect the mechanisms controlling growth and size of the *Drosophila* wing, and have mostly focused on the distribution and regulation of cell proliferation while neglecting cell death [15-19, 21]. Indeed, seminal works more than 20 years ago found that cell death is relatively minor in the wing disc and that it occurs sporadically without any noticeable pattern [23]. Similarly, recent systematic tracking of cells in the pupal wing during elongation (between 16 and 32 hours after pupal formation, APF) suggested that apoptosis has also a minor role for wing elongation at the pupal stage [27, 40]. Yet, these works did not exclude more subtle functions of cell death.

Accordingly, apoptosis was proposed to buffer developmental fluctuations to ensure reproducible wing size [41]. This was assumed to be based on cell competition: the context dependent elimination of suboptimal cells from growing tissues [42, 43]. Interestingly, while the studies of cell competition are mostly based on the analysis of

mutant clone disappearance in the wing disc, we know very little about spontaneous clone disappearance during normal wing development and the prevalence, localisation and functions of physiological cell competition. Recently, apoptosis was proposed to fine tune of Dpp gradient shape by eliminating supernumerary cells to match gradient decay length and tissue size [12]. Alternatively, basal sublethal effector caspase activity was also proposed to modulate global wing growth and size [44]. These results call for a reassessment and more thorough characterization of cell death in the wing and its contribution to growth and tissue shape.

Here, we performed systematic mapping of apoptosis using various markers of caspases and apoptosis, together with spatial registration in the larval wing imaginal disc. Unexpectedly, we found striking reproducible biases in the distribution of cell death which outlined hot-spots of apoptosis. These hot-spots correlate with a local increase of clone disappearance probability and significantly reduce local net-growth in the wing disc. Using live imaging of the pupal wing, we also showed that these spatial biases persist at early pupal development and that new spots of apoptosis appear later during development. Finally, using morphometric analysis, we further demonstrate that these hot-spots can tune adult wing size and shape. Altogether, we reveal that apoptosis cannot be neglected for the study of growth/size and is also an essential modulator of local shape and growth even in a fast-expanding tissue. Our study also proposes a roadmap for a more systematic characterisation of the contribution of cell death to clone dynamics and tissue growth.

Results

Caspase activity and apoptosis are spatially biased in the larval wing pouch

We first systematically evaluated the distribution of apoptotic cells in the *Drosophila* wing disc at the larval wandering stage (96 h After Egg Laying - AEL). We used the live effector caspase reporter GC3Ai [45] driven in the larval pouch and hinge by the driver GMR11F02-GAL4 (**Figure 1C**). The brightest GFP spots revealed by the reporter correspond to cell debris located on the basal sides, thus staining cells which already extruded ([45], **Figure 1D**). We confirmed the accuracy of the GC3Ai marker as we obtained a similar pattern with cleaved caspase3 staining (cleaved DCP1), although this was less sensitive and fails to mark the cells with faint GC3Ai signal (**Figure 1suppE-G'**). Moreover, bright GC3Ai dots used for the analysis colocalized

with TUNEL positive cells (**Figure 1suppE-G'**), confirming that they marked late apoptotic cells. To obtain an averaged map of the spatial distribution of cell death, we used spatial landmarks, whose positions were defined by the intervein marker Drosophila Serum Response Factor (DSRF, **Figure 1D,E**). The landmarks positions were used to divide every dissected wing disc into 40 sub-compartments (**Figure 1suppA-D**). In addition, we applied procrustes transformation (translation, rotation and scaling) on landmarks positions to align the discs and superimpose GC3Ai/Dcp1/TUNEL spatial data from many individuals on a single image (see **Methods**). The averaged distribution of apoptotic cells revealed a striking non-homogenous distribution of apoptosis with the strongest "hot spot" located in the anterior - dorsal quadrant, near the dorsal-ventral boundary (**Figure 1 F,G**, $p<0.001$, Moran autocorrelation spatial test, null hypothesis being an homogenous distribution with no spatial correlation). This bias is not driven by the Gal4 driver or any side effect of GC3Ai as a similar pattern was obtained in the w^- background with cleaved caspase3 staining (**Figure 1suppH,I**) or with TUNEL staining (**Figure 1suppJ,K,** Moran's p-value=0.007). To check whether the spatial bias of GC3Ai signal persists during wing disc development, we also monitored GC3Ai-positive cells in the early L3 wing disc (72h AEL). As we could not use the same spatial landmarks (the intervein regions are not yet defined at this stage) we instead used the location of the 4 compartments defined by AP and DV compartment boundaries (Anterior, Posterior, Dorsal and Ventral) as a spatial reference. The number of apoptotic cells was more than two times higher in the anterior-dorsal compartment than in the others (**Figure 1J-L** pairwise t-test p-values ≤ 0.056). This suggested that the spatial bias emerges at least during early L3 stage and persists for more than 24 hours. We then checked whether this pattern was indeed dependent on core regulators of apoptosis/caspases. Co-expression of GC3Ai with a dominant negative allele of Dronc (*Drosophila* caspase9) significantly reduced the amount of GC3Ai signal and reduced the spatial bias (**Figure 1H**, **Figure 1suppL-N, S**). Similarly, depletion of the pro-apoptotic gene *hid* by RNAi in the wing pouch almost completely abolished the GC3Ai signal (**Figure 1I**, **Figure 1suppO-Q, S**). Finally, the number of TUNEL positive cells was significantly reduced in a $dark^{[CD4]}$ mutant background (Drosophila Apaf1/Apoptosome protein[46]) specifically in the apoptosis hotspots regions (**Figure 1suppR,R',T**, compared with **1suppK**). These observations suggest that the spatial bias is at least in part caspase-dependent and most likely relies on the expression of the pro-apoptotic gene *hid* and

on the apoptosome. Accordingly, we found a slight but systematic and reproducible increase of *hid* expression near the GC3Ai hot spot region using a GFP insertion at the *hid* locus (**Figure 1M,N**). Note however that other factors may also contribute to the spatial bias as we still observed some heterogeneity in cell death distribution upon Dronc inhibition or *hid* depletion (**Figure 1suppN, Q, S**) [12]. We also checked the pattern of expression of other pro and anti apoptotic genes, namely *reaper*, *grim* and *diap1* (**Figure 2supp A-C'**). While none of them matched specifically the full pattern of apoptosis, we did find some partial overlap between local increase of apoptosis in the proximal intervein L3-L4 regions of the disc and *reaper* expression (**Figure 2supp A,A'**). This suggested that the pattern of apoptosis strongly relies on *hid*, but may be influenced by the pattern of expression of other core regulators of apoptosis.

Altogether, we conclude that contrary to what was previously observed [12, 23] apoptosis is not spatially homogeneous in the wing imaginal disc and that some regions (anterior and close to the DV boundary, dorsal compartment) undergo higher rates of apoptosis. These hot-spots are in part explained by a spatial bias in the expression of the pro-apoptotic gene *hid* but are also likely to be regulated by other factors.

The spatial bias in apoptosis influences clonal disappearance and local net-growth.

We next checked whether this spatial bias in apoptosis could have any consequence on clonal dynamics and local growth. Since *ex-vivo* live imaging of the wing disc does not allow long-term tracking of cell fate and local growth, we used an alternative approach based on twin-clone labelling. We used the QMARCM technique [47] to stain the two daughter cells generated after mitotic recombination and their progeny with different fluorescent markers using alternate sets of transcription factors (Gal4 or the Qsystem, **Figure 2A,B**). Since cell movements and cell-cell intercalations are relatively neglectable in the wing disc [48, 49], the spatial proximity of patches of cells marked with GFP and RFP can be unambiguously attributed to a twin-clone in conditions of low frequency of clone induction. We assessed the probability of clone disappearance by scoring the number of single-coloured clones which are not in the vicinity of the other sibling clone 48h after clone induction. Such an observation can only be explained by the early disappearance of the lineage of the other daughter cell, and thus identifies a clone disappearance event (**Figure 2A**). We first noted that the

QMARCM system has an intrinsic bias towards smaller clones and higher probability of clone disappearance for GFP/Gal4 clones relative to RFP/QF ones (**Figure 2suppD**), most likely due to the inherent toxicity of Gal4 [50]. While in this context we cannot extrapolate on the absolute probability of clone disappearance, this however should not preclude the analysis of potential spatial biases. By multiplexing a large number of discs and using the same spatial landmarks as those used in **Figure 1suppC** (**Figure 2B**), we obtained a coarse-grained spatial map of the probability of clone disappearance (**Figure 2C**). Strikingly, we observed that similar to caspase activation in the tissue, the probability of clone disappearance is not spatially homogenous (Moran's test p-value <0.001). We identified clear hot-spots of clone death, including the anterior-dorsal region near the DV boundary (~two-fold increase compared to posterior compartments at similar DV positions, **Figure 2C, 2suppE**), as already outlined by the caspase positive cells mapping (**Figure 1G**). Note that this clone strategy reflects the pattern of apoptosis at earlier stages of development (most likely around the time of clone induction, early L2) compared to the one revealed with apoptotic markers. Nevertheless, we still observed a significant compartment to compartment correlation between GC3Ai levels and clone disappearance probability (weighted Pearson's correlation=0.38, p=0.016). Importantly, clone size was also on average smaller (estimated through total apical surface and number of cells) in regions showing high rates of apoptosis and clone disappearance (**Figure 3A, Figure 3suppC**). This suggested that spatial biases in caspase activity not only modulate the probability of clone survival, but also the cumulative local growth in the wing disc. Indeed, these local differences in clone size match the differences numerically estimated from an exponential growth model with no spatial difference in proliferation rate and including the spatial differences in apoptotic rates calculated from our measurements of clone disappearance (see **Methods, Figure 3B-D**). This indicates that local differences in clone size could be solely explained by spatial differences in apoptotic rates. To check whether these spatial differences are indeed driven by caspases, we repeated the QMARCM clonal assay upon inhibition of caspase in the Gal4 sibling clones (using UAS-Dronc^{DN}). While this did not totally abolish clone disappearance, the spatial pattern was flattened with no visible hot-spot of clone disappearance in the anterior side (**Figure 2C', 2suppE**, Moran's test p-value = 0.11, no significant spatial bias; Pearson's correlation with WT QMARCM single clone pattern = 0.078, p=0.63) and led to a more homogenous clone size between anterior

and posterior compartment (**Figure 3suppD**). To confirm the effect of caspases and to check whether a similar pattern could be observed in absence of Gal4, we also used mitotic clones in the H99/+ background (a deletion covering the three pro-apoptotic genes *hid*, *grim* and *reaper* [51]) generating on the one hand H99 homozygous mutant clones (resistant for apoptosis) as well as a WT siblings. While we observed globally less single clones compared to the QMARCM approach (confirming the impact of Gal4 on clone disappearance probability), single H99 clones (loss of WT sibling) were markedly more frequent near the hotspots of apoptosis (**Figure 2D**, Moran's test for spatial autocorrelation: p=0.003, Pearson's correlation with GC3Ai pattern: 0.41, p=0.009), and completely biased toward WT clone disappearance. This confirmed the pattern of clone disappearance observed with QMARCM in absence of any possible bias caused by Gal4 toxicity. H99 mutant clones were almost systematically larger than their WT siblings (**Figure 3E**, 30,8% larger on average, t-test p-value < 0.0001), and this bias was notably high in the hotspot of apoptosis in the margin region at the intervein L2-L3 region (Ratio=0.24, n=72) (**Figure 3F, 3suppE,F**). Induction of neutral mitotic clones (marked with 2 copies of EGFPnls versus 2 copies of β-gal) on the contrary shows an almost perfectly symmetric distribution of clone size between the two siblings with no asymmetry of probability of clone disappearance, and yet a similar global probability of clone disappearance compared to WT clones in H99/+ background (7 % versus 8,2 %, **Figure 2 supp F,G, Figure 3 supp G,H**). Moreover, we could also recapitulate a similar spatial bias of clone disappearance and clone size (**Figure 2 Supp G, Figure 3 Supp G**). Altogether, this confirmed that *i)* the spatial bias of clone disappearance can also be observed in absence of Gal4, *ii)* clone disappearance is apoptosis dependent and *iii)* apoptosis has a net negative impact on local growth especially in the apoptotic hotspots regions (**Figure 1**).

Altogether, we conclude that the spatial bias in apoptosis generates hotspots of clone disappearance which also significantly reduces local growth rate mostly in the anterior-dorsal region near the DV boundary. This suggests that local increases of apoptosis could play an instructive role in significantly modulating local growth, which therefore may affect the final shape and size of the tissue.

Patterned apoptosis in the larvae and in the pupae modulate adult wing shape and size

We therefore checked whether local biases in apoptosis could significantly impact adult wing shape and size. To obtain a precise and quantitative description of adult wing shape and size, we used a quantitative assay based on semi-automatic wing segmentation, landmark positioning and procrustes alignment of wings (which includes translation, rotation and global rescaling) [52, 53] (**Figure 4suppA**). To analyse the impact of apoptosis in the wing proper, we used the Nab-Gal4 driver, one of the few drivers well restricted to the pouch both at larval and pupal stage (**Figure 4A**). Interestingly, inhibition of cell death in the wing tissue using *hid* RNAi or a microRNA targeting *hid*, *grim* and *reaper* (mirRHG [54]) led to a significant increase in wing size (**Figure 4B,C** 8.7% and 4.2% respectively, a similar range to what was obtained upon ectopic overexpression of Dp110/PI3K [55]), suggesting that apoptosis has a net negative effect on adult tissue size. Hid-dsRNA and mirRHG effect on hid mRNA levels was confirmed by RT-PCR (see Star Methods). We also observed significant changes to adult wing shape, including a relative increase in the size of the most anterior and posterior domains, as well as a global wing rounding (**Figure 4D**). To check whether local increases in apoptosis were indeed responsible for the local modulation of shape and size, we used various drivers to inhibit apoptosis in different wing subdomains (**Figure 4E**). Accordingly, inhibition of *hid* in the patched domain (*ptc-gal4*, expressed in a band at the intervein L3-L4, **Figure 4E**) led to a global increase of wing size characterised by the expansion of the region overlapping the *ptc* domain (**Figure 4F,G**). This suggested that apoptosis has a local impact on growth even in regions other than the apoptosis hot-spots identified at larval stage. We also used drivers restricted to the DV boundary either in the anterior (*aristaless-GAL4*, encompassing the caspase hot-spot) or posterior part of the wing disc (*trithorax-GAL4*) (**Figure 4G**). Interestingly, while *hid* depletion in the posterior-DV boundary domain had a mild effect on wing size (**Figure 4F,G**, 2.1%, similar to inhibition of *hid* in the ptc domain), this effect was enhanced upon inhibition in the anterior-DV boundary domain (4.1%, **Figure 4F,G**). Importantly, the expansion of the most anterior domain of the wing was only observed upon inhibition of *hid* in the anterior-DV boundary domain (**Figure 4F,G**). Altogether, this suggests that apoptosis has a local negative effect on wing domain size which is more significant in regions overlapping hotspots of apoptosis characterized in the wing imaginal disc.

So far, our perturbative approaches did not allow to distinguish the contributions of apoptosis during larval or pupal stage, where significant tissue size and shape modulation can still take place [27, 36, 37, 56]. Therefore we also performed experiments with conditional *hid* depletion under the control of a temperature sensitive driver (Gal4 combined with Gal80^{ts}) to assess the relative contribution of *hid* expression at larval stage versus pupal stage to the final wing shape and size (**Figure 4suppB,C**). Despite the strong confounding effect of temperature on wing size [57], we found that *hid* depletion at larval stage (up to mid L3) had a significant impact on adult wing size (**Figure 5A**, larval expression, +7%, t-test p-value < 0.001) while depletion during pupal stage had a milder effect (**Figure 5A**, pupal expression, +2.9%, similar to the background effect observed in the negative control, +3.4 %, the absence of significant effect was confirmed by bootstrapping).This suggested that larval apoptosis had a significant negative contribution to global wing size. We then analysed the relative contribution of larval and pupal apoptosis to final adult wing shape. Surprisingly, this revealed that the wing shape modulation observed upon persistent *hid* downregulation could be partially recapitulated by pupal inhibition of *hid* (compare **Figure 5B** pupal expression and full expression, to **Figure 4D),** suggesting that pupal apoptosis also contributes to adult wing shape. We next used PCA (Principal Component Analysis) to decompose the main contributors of shape variation and compare unambiguously and quantitatively wing shape between conditions. Removing the effect of temperature (Principal Component 1) outlined the contribution of shape variation (Principal Component 3) which is going along the same direction for larval, pupal and full depletion of Hid (**Figure 5SuppA,B**). Interestingly, the amplitude of variation along PC3 for Hid full depletion matches the sum of variations observed for larval and pupal depletion, suggesting that adult wing shape is generated by the cumulative effect of larval and pupal inhibition of apoptosis, which have similar effects on shape. Variations along PC3 mostly recapitulates global wing rounding (**Figure 5SuppC** wing deformation between the two extreme values along PC3) in good agreement with the shape modulation observed for Hid depletion throughout development (**Figure 4B,D**).

This prompted us to evaluate the pattern of apoptosis in the pupal wing. We performed live imaging of pupal wings between 16h and 35h APF (After Pupal Formation) expressing GC3Ai in the pouch (using the Nab-Gal4 driver). This revealed striking

dynamics of apoptosis with an early concentration in the most anterior part of the wing as well as the junction with the hinge (**Figure 5C, Video S1**). This pattern shows an interesting correspondence with the hotspots observed at larval stage (**Figure 5C-D'**) suggesting that the spatial biases present at larval stage are for a good part maintained during pupal development. Nevertheless, the pattern of apoptosis is dynamic as new hotspots of apoptosis appear at later (~30 h APF) pupal stage (**Figure 5C,D'**) Importantly, the domains of high GC3Ai expression and apoptosis match the regions more significantly deformed in the adult wing upon pupal inhibition of Hid (compare **Figure 5C-D'' Video S1**). Using ubiquitous expression of GC3Ai driven by lexA, we also confirmed that larval expression of hid-dsRNA using Nab-Gal4 and Gal80ts does not impact caspase activity in the pupal wing blade, while pupal expression of hid-dsRNA reduced GC3Ai signal in the pupal wing blade (**Figure 5supp D,E**).

Altogether, we conclude that spatial biases in apoptosis distribution in the growing wing can significantly modify the size and shape of the adult wing, by modulating morphogenesis either during early larval stages or during later pupal ones. This suggests that the fine spatial tuning of apoptosis in a fast-growing tissue plays an instructive role for organ shape and size regulation.

Discussion

In this study, we outlined an unexpected pattern of apoptosis in the growing wing imaginal disc with a significant upregulation in the anterior and dorsal compartment of the wing. Part of this pattern is preserved during pupal stage and contributes to pupal wing morphogenesis. Moreover, our quantitative assessments of clonal growth and adult wing shape clearly show that this local upregulation of apoptosis has a significant impact on local net growth and final adult shape and size. Most likely, local upregulation of apoptosis fine tune wing shape by locally reducing the number of cells and altering the relative proportion of wing subdomains, although nothing excludes at this stage more complicated contribution through an apoptosis-dependent modulation of tissue mechanics and/or signaling pathways. So far, the characterisation of cell death has never been performed in a systematic manner using spatial landmarks allowing superimposition of data from many individuals, which may explain why such biases have been missed [23]. Similarly, the impact of apoptosis on tissue shape and size has never been studied with such quantitative readouts. Our work emphasises the need

for more systematic quantitative assessments of death distribution in order to evaluate its contribution to organ shape/size regulation. The pipeline used in this study may easily be applied in other developmental contexts which are not amenable for long term live imaging, as long as markers can be used for spatial registration and tools are available for clone generation.

Previous work suggested that sublethal caspase activation also contributes to wing disc growth regulation and adult tissue size, however in this situation basal caspase activity promotes growth and effector caspase inhibition through p35 overexpression rather reduces wing size[44]. This effect however is not visible upon inhibition of upstream regulators of caspases, which was interpreted by the absence of inhibition of the pro-growth basal effector caspase activity. In this study, we purposively used upstream inhibitors of apoptosis to avoid this effect, which revealed now an increase of local growth and wing size upon apoptosis inhibition. Our preliminary observation in the pupal wing also suggests the existence of a significant proportion of cell death in the hinge region (**Video S1, Figure 5 C-D''**). Interestingly, our preliminary observations using hinge specific driver suggests that apoptosis inhibition in the hinge rather reduces adult wing size (not shown). This is in sharp contrast with the effect we observed upon inhibition in the pouch and suggest that the interpretation of wing shape phenotype requires to precisely monitor the domains of perturbations, especially for commonly used Gal4 encompassing both pouch and hinge region (e.g.: nubbin-Gal4). While we focused here on tissue autonomous contribution of cell death, future work will help to decipher the putative contribution of hinge apoptosis to final wing size and shape through a non-tissue autonomous effect.

Compensatory proliferation is one of the best studied processes that relates apoptosis to the induction of cell proliferation [58]. So far, this process was mostly characterised either in conditions of massive death induction through irradiation and genetic induction of apoptosis in large domains [59, 60], or through the perturbation of the core apoptotic pathway (e.g.: by blocking some of the essential caspases, caspase3 in *Drosophila* [61], or caspase9 in mammalian epidermis [62]). However, to our knowledge there is no study that has clearly identified biases in cell proliferation distribution in the vicinity of physiological apoptosis *in vivo*. Surprisingly, we observed a net negative effect of the local increase of cell death on local growth and the size of the final adult compartment, and also outlined a significant effect of physiological death on the final

size of the adult wing (**Figure 2** and **Figure 4**, **Figure 5**). This suggests that compensatory proliferation is unlikely to occur in the context of physiological apoptosis, or at least that its contribution is relatively minor and not sufficient to compensate for cell loss by apoptosis. Further quantitative studies of the coupling between apoptosis and cell proliferation will be essential to assess its real contribution to physiological growth regulation. Interestingly, a recent study outlined a significant positive upregulation of proliferation near dying MDCK cells, however this effect is strongly context-dependent and is not visible at low stiffness or high density values [63], conditions that may apply to the wing imaginal disc.

Cell competition is the process describing the context-dependent elimination of viable but suboptimal cells [6]. Studies of clonal elimination in the wing imaginal disc have thoroughly contributed to our understanding of this process. Interestingly, most of these studies assumed that clone disappearance in physiological conditions is largely neglectable. Our results suggest that WT clones can undergo early elimination in the wing imaginal disc, and that this elimination is spatially biased, although we should remain cautious when extrapolating the absolute probability of clone elimination compared to the experimental conditions used in this study. On the one hand, this opens the possibility for spontaneous competition occurring in the wing imaginal disc, which so far has not been thoroughly explored (although its existence has been suggested by indirect genetic evidence [12, 41, 64]). On the other hand, it also suggests that cell elimination during competition may be influenced by this spatial pattern of caspase activity and apoptosis. Further quantitative description of clonal elimination during competition may reveal such spatial bias and would help to study the influence of pre-existing patterns of caspases/apoptosis on cell competition and tissue plasticity.

In this study, we showed that local modulation of *hid* expression can fine-tune the local level of apoptosis which will impact local growth and adult tissue shape in a subtle and quantitative way, similarly to the phenotypic changes observed at the macroevolutionary scale [65]. As such, the evolution of the cis-regulatory elements of pro-apoptotic genes may constitute an additional lever for shape evolution that could be used to fine tune adult appendage shape. It would be important in this perspective to understand which factors fine tune the expression levels and the pattern of pro-apoptotic genes and dissect how they might be modulated during evolution.

Interestingly, these pro-apoptotic genes are most likely less pleiotropic than pro-proliferative pathways such as morphogens, RTK signaling pathways, or Hippo pathways that are classically studied for the regulation of size and growth [15]. As such, modulating pro-apoptotic genes levels and pattern of expression may constitute a relatively parsimonious way to evolve wing and appendage shape.

Acknowledgements

We thank members of RL lab for critical reading of the manuscript. We would like to thank Christina Fissoun, Lucia Rodriguez Vazquez, Gaurav Shajepal and Delia Cicciarello for their contribution to adult wing and wing disc analysis during their internship. We are also grateful to Jean-Paul Vincent, Magali Suzanne, David Houle, Seth Blair, Andrea Bergman, Yohanns Bellaïche, Jae Park, the Bloomington Drosophila Stock Center, the Drosophila Genetic Resource Center and the Vienna Drosophila Resource Center, Flybase for sharing essential information, stocks and reagents. We also thank Benoît Aigouy for the Packing Analyser software, Raphaël Etournay for very helpful guidance on pupal wing live imaging, and Jean-Yves Tinevez and the image analysis platform of Institut Pasteur for the LocalZprojector plugin on Fiji. Work in RL lab is supported by the Institut Pasteur (G5 starting package), the ERC starting grant CoSpaDD (Competition for Space in Development and Disease, grant number 758457), the ANR-10-LABX-0073, the Cercle FSER and the CNRS (UMR 3738).

Authors contribution

RL and AMV discussed and designed the project and wrote the manuscript. TC performed part of the experiments on adult wing shape and twin clones analysis as well as the wing disc segmentation. FL participated to adult wing dissection, imaging and segmentation, performed the RT-PCR and generated the lexAOP-GC3Ai line. AD provided the theoretical calculation of the expected distribution of clone size based on differences in apoptotic rates. AMV performed all the other experiments and analysis. Every author has commented and edited the manuscript.

Declaration of interests

The authors declare no competing interest

Star Methods

Resource availability

Lead contact

Further information and requests for resources and reagents should be directed to and will be fulfilled by the lead contact, Romain Levayer (romain.levayer@pasteur.fr).

Material availability

All the reagents generated in this study will be shared upon request to the lead contact without any restrictions.

Data and Code availability

All code generated in this study and the raw data corresponding to each figure panel (including images) can be shared upon request and will be uploaded to a repository following acceptance.

Experimental model and subject details

Drosophila melanogaster husbandry

All the experiments were performed using *Drosophila melanogaster* fly lines (listed in **Table 1**) breed with regular husbandry techniques. The fly food used contains agar agar (7.6 g/l), saccharose (53 g/l) dry yeast (48 g/l), maize flour (38.4 g/l), propionic acid (3.8 ml/l), Nipagin 10% (23.9 ml/l) all mixed in one liter of distilled water. Flies were raised at 25°C in plastic vials with a 12h/12h dark light cycle at 60% of moisture unless specified in the legends and in the table below (alternatively raised at 18°C or 29°C). Females and males were used without distinction for all the experiments, except for the adult wing shape analysis in which only left wings from female flies were used. We did not determine the health/immune status of pupae, adults, embryos and larvae, they were not involved in previous procedures, and they were all drug and test naïve.

Drosophila melanogaster strains

The strains used in this study and their origin are listed in the table 1 below.

Fly line	Chromosome location	Origin (citation)	RRID

UAS-GC3Ai /TM6b	III	[45], Magali Suzanne	none
w; UAS-GC3Ai/Cyo ; MKRS/TM6b	II	Bloomington and [45]	BDCS_84346
UAS-hid dsRNA	III	VDRC	GD 8269
UAS-lacZ	II	Bloomington	BDCS_8529
UAS-dronc^{DN}	II	Boomington	BDCS_58992
GMR11F02-gal4	III	Bloomington	BDCS_48928
w^{118}	X	Bloomington	BDCS_3605
UAS-dicer2 ; nubbin-gal4	X, II	Bloomington	BDCS_25754
w; ; hid$^{\Delta.GFP}$/TM3	III	[66], Jean-Paul Vincent	none
yw; ET40-QF, QUAS-tdTomato; FRT82B, tub-QS	X, II, III	Bloomington	BDCS_30042
yw, hs-flp22, UAS-GFP ; if/Cyo ; tub-gal4, FRT82B, tub-gal80/TM6b	X, III	This study and Bloomington	BDCS_86311
yw; UAS-mCd2RFP , UAS-dsRNACD8 FRT40A ; TM3/TM6b	II, III	Bloomington	BDCS_56184
yw; UAS-mcd8GFP, UAS-dsRNACD2 FRT40A ; TM3/TM6b	II, III	Bloomington	BDCS_56185
w; ptc-gal4	II	Bloomington	BDCS_2017
w; GMR83F09-gal4	II	Bloomington	BDCS_40367
w; GMR36C06-gal4	II	Bloomington	BDCS_49931
w; tub-gal80ts	II	Bloomington	BDCS_7108
w; UAS-lacZ	II	Bloomington	BDCS_8529
w; ; rpr-LacZ	III	Bloomington	BDCS_58793
w; ;grim-gal4	III	Bloomington	BDCS_29117
w; ; diap1-LacZ	III	Bloomington	BDCS_12093
w; 20xUAS-EGFPx6	II	Bloomington	BDCS_52261
w; ; Df(3L)H99 FRT80B/TM2	III	Andrea Bergman	none
yw hs-flp22; ; arm-βgal FRT80B	III	Bloomington	BDCS_6341
w; ; ubi-EGFPnls FRT80B	III	Bloomington	BDCS_5630
w; ; nab-Gal4	III	DGRC Kyoto	DGRC_104533
w; UAS-miRHG	II	Jae Park[54]	none
yw; p(LacW)Dark$^{[CD4]}$	II	Bloomington	BDCS_23286
w; E-cad::3XmKate(KI)/Cyo GFP	II	Yohanns Bellaïche [67]	none
w; lexAOP-GC3Ai	II	This study	This study

w; act-lexA	II	Bloomington	BDCS_62567

Table 1 : description and origin of the *Drosophila melanogaster* strains used in this study.

The exact genotype used for each experiment is listed in table 2

Figure	Genotype	Clone induction	Dev. time
1 A-G, J-L	*w; + ; GMR11F02-gal4/UAS-GC3Ai*	-	96h AEL
1 H	*w; UAS-dronc^{DN}/+ ; GMR11F02-gal4/UAS-GC3Ai*	-	96h AEL
1 I	*w; UAS-GC3Ai/+ ; GMR11F02-gal4/ UAS-hid-dsRNA*	-	96h AEL
1 J-L	*w; + ; GMR-11F02-gal4/UAS-GC3Ai*	-	72h AEL
1 M,N	*w ; + ; hid$^{\Delta GFP}$/TM3*	-	96h AEL
1supp A-G',S	*w; + ; GMR11F02-gal4/UAS-GC3Ai*	-	96h AEL
1supp H-K	*w^{118}*	-	96h AEL
1supp R,R',T	*w; dark$^{[CD4]}$/dark$^{[CD4]}$*	-	96h AEL
1supp L-N,,S	*w; UAS-dronc^{DN}/+ ; GMR11F02-gal4/UAS-GC3Ai*	-	96h AEL
1supp O-Q,S	*w; UAS-GC3Ai/+ ; GMR11F02-gal4/UAS-hid-dsRNA*	-	96h AEL
2B, 2C, 2suppD,E	*yw hs-flp22, UAS-GFP/+; ET40-QF, QUAS-tdTomato/Cyo-If; FRT82B, tub-QS/FRT82B, tub-gal80*	8 min hs, 48h ACI	96h AEL
2D	*yw hs-flp22/+; ; arm-βgal FRT80B/ Df(3L)H99 FRT80B*	12 min hs, 48h ACI	96h AEL
2supp A,A'	*w; ; rpr-LacZ*	-	96h AEL
2supp B,B'	*w ; ; diap1-LacZ*	-	96h AEL
2supp C,C'	*W ; UAS-EGFPx6/+ ; grim-Ga4/+*		96h AEL
2supp D,E	*yw hs-flp22, UAS-GFP/+; ET40-QF, QUAS-tdTomato/Cyo-If; FRT82B, tub-QS/FRT82B, tub-gal80* *yw hs-flp22, UAS-GFP/+; UAS-dronc^{DN}/ET40-QF, QUAS-tdTomato; FRT82B, tub-QS/FRT82B, tub-gal80*	12 min hs, 48h ACI	96h AEL
2supp F,G	*yw hs-flp22/+; ; arm-βgal FRT80B/ ubi-EGFPnls FRT80B*	12 min hs, 48h ACI	96h AEL
3A-D	*yw hs-flp22, UAS-GFP/+; ET40-QF, QUAS-tdTomato/Cyo-If; FRT82B, tub-QS/FRT82B, tub-gal80*	8 min hs, 48h ACI	96h AEL
3E,F	*yw hs-flp22/+; ; arm-βgal FRT80B/ Df(3L)H99 FRT80B*	12 min hs, 48h ACI	96h AEL
3supp A-C	*yw hs-flp22, UAS-GFP/+; ET40-QF, QUAS-tdTomato/Cyo-If; FRT82B, tub-QS/FRT82B, tub-gal80*	8 min hs, 48h ACI	96h AEL
3supp D	*yw hs-flp22, UAS-GFP/+; UAS-dronc^{DN}/ET40-QF, QUAS-tdTomato; FRT82B, tub-QS/FRT82B, tub-gal80*	8 min hs, 48h ACI	96h AEL
3supp E,F	*yw hs-flp22/+; ; arm-βgal FRT80B/ Df(3L)H99 FRT80B*	12 min hs, 48h ACI	96h AEL
3supp G,H	*yw hs-flp22/+; ; arm-βgal FRT80B/ ubi-EGFPnls FRT80B*	12 min hs, 48h ACI	96h AEL
4A	*w; UAS-EGFPX6/E-cad:mKateX3; Nab-Gal4/+*	-	96h AEL and 18hAPF
4B-D	*w; UAS-lacZ/+; Nab-Gal4/+*	-	adult
4B-D	*w; ; UAS-hid dsRNA/Nab-Gal4*	-	adult
4E	*w; UAS-lacZ/aristaless-gal4*	-	96h AEL

4E	*w; UAS-lacZ/trithorax-gal4*	-	96h AEL
4E	*w; UAS-lacZ/ptc-gal4*	-	96h AEL
4F,G	*w; UAS-lacZ/aristaless-gal4; +*	-	adult
4F,G	*w; aristaless-gal4/+; UAS-hid dsRNA/+*	-	adult
4F,G	*w; UAS-lacZ/trithorax-gal4; +*	-	adult
4F,G	*w; trithorax-gal4/+; UAS-hid dsRNA/+*	-	adult
4F,G	*w; UAS-lacZ/ptc-gal4 ; +*	-	adult
4F,G	*w; ptc-gal4/+ ; UAs-hid dsRNA/+*	-	adult
4supp A	w^{118}	-	adult
5A,B	*w; UAS-lacZ/tub-gal80^{ts}; Nab-Gal4-gal4/+*	-	adult
5A,B	*w; +/tub-gal80^{ts}; Nab-Gal4/UAS-hid dsRNA*	-	adult
5C-D	*w; E-cad:mKateX3/UAS-GC3Ai; Nab-Gal4/+*	-	pupae 15-30h APF
5supp A-C	*w; UAS-lacZ/tub-gal80^{ts}; Nab-Gal4-gal4/+*	-	adult
5supp A-C	*w; +/tub-gal80^{ts}; Nab-Gal4/UAS-hid dsRNA*	-	adult
5 supp D,E	*w; act-lexA, lexAOP-GC3Ai/UAS-lacZ; Nab-Gal4-gal4/ tub-gal80^{ts}*	-	pupae ~25h APF
5 supp D,E	*w; act-lexA, lexAOP-GC3Ai/tub-gal80^{ts}; Nab-Gal4/UAS-hid dsRNA*	-	pupae ~25h APF

Table 2: genotype used for each experiment. AEL: after egg laying; hs : heat shock duration at 37°C; ACI : time after clone induction.

Design of lexAOP-GC3Ai fly line

p13xLexAop2-GC3AI was generated by PCR-amplifying GC3Ai from pCDH-puro-CMV-GC3AI (Addgene 78910) and cloned in pJFRC19-13XLexAop2-IVS-myr::GFP (Addgene 26224) cut with NotI and XbaI (to excise myr::GFP) and inserted using In-Fusion assembly method. The construct was checked by sequencing and inserted at the attp site attp40A after injection by Bestgene.

The following primers were used for GC3Ai amplication:

GC3AI_F: ATCCTTTACTTCAGGCGGCCGCGAATTGCCACCATGTACCCCTA

GC3AI_R: ACAAAGATCCTCTAGACTTACAGGTCCTCCTCGCTGAT

QPCR validation of Hid depletion

Hid depletion by RNAi and microRNA was validated by RTPCR. Total RNA was prepared from wing imaginal disc expressing hid-dsRNA or mirRHG under the control of the Nab-Ga4 driver (non-Tb larvae) using TRIzol reagent (Invitrogen). RNA (1ug) was retrotranscribed using random primers and Superscript III reverse transcriptase (Invitrogen). cDNA was analyzed by qPCR using FastStart Universal SYBR Green

(Roche) and Actin-42A was used as a reference gene. The primers used for Actin 42A and Hid amplifications were the following:

Actin 42A_F: GAGCGCGGTTACAGCTTCA

Actin 42A_R: TCCTTGATGTCGCGCACA

Hid_F: GTACCAGAGCCAGCAGAGTG

Hid_R: GCGGATGGGGATTCGAGTTC

All assays were performed in triplicate, and mean values were calculated according to the ΔCT quantification method. Results are expressed as the average from at least three independent experiments normalised to the control condition (Nab-Gal4, UAS-lacZ). Doing so, we obtained an average Hid mRNA level at 0.59 for mirRHG versus 0.46 for hid dsRNA (p=0.02), suggesting a very efficient depletion in both cases, but more efficient for hid dsRNA.

Immunostaining

Dissections of larval wing imaginal discs were performed on PBS in ice. Dissected discs were fixed for 20 min in 4 % formaldehyde (SIGMA F8775), rinsed 3 times in PBT (PBS 0.4 % Triton), followed by 10 min permeabilisation in PBT. Primary and secondary antibodies were incubated for 2 h at room temperature (or 12 h at 4 °C) under rocking agitation. After each antibody incubation, discs were rinsed 3 times in PBT, followed by 3 washes of 30 min. Discs were mounted in Vectashield® (EUROBIO SCIENTIFIC / H-1000) and imaged using a confocal spinning disc microscope (Gataca systems) with a 40X oil objective or a LSM880 equipped with a fast Airyscan using a 40X oil objective. The following primary antibodies were used: rat anti E-cadherin (1/100, DCAD2 concentrated DSHB), mouse anti DSRF (1/500, gift of Seth Blair), rat anti Delta (1/1000, gift of François Schweisguth), chicken anti GFP (1/1000, abcam ab13970), rabbit anti RFP (1/500, abcam 62341), rabbit anti DCP-1 (1/100, Cell Signaling 9578S), chicken anti Beta-gal (1/1000, Abcam ab 9361), mouse anti Wingless (1/250, 4D4 concentrated DSHB), mouse anti Patched (1/250, Apa-1 concentrated, DSHB), phalloidin alexa 647 (1/50, Invitrogen). Secondary antibodies were: anti rabbit alexa 555 (1/500, Invitrogen), anti chicken alexa 488 (1/500, Invitrogen), ultrapurified anti mouse 405 (1/500, Jackson ImmunoResearch / 715-476-151), ultrapurified anti mouse Cy3 (1/500, Jackson ImmunoResearch / 715-165-151),

ultrapurified anti rat Cy3 (1/500, Jackson ImmunoResearch / 712-165-153), ultrapurified anti rat alexa 647 (1/500, Jackson ImmunoResearch / 712-605-153). TUNEL assays for the detection of dying cells with fragmented DNA were conducted using the *In Situ Cell Death Detection Kit, TMR red* (Roche diagnostics®) and the *TUNEL dilution buffer* (Roche diagnostics®), following the experimental procedure described in [68].

Image processing

All images were processed using FIJI[69] . For the twin clones analyses, Z projections of z-stacks were done using the Fiji LocalZProjector plugin using E-cad or phalloidin staining as a reference plane[70], allowing to project a limited number of planes around the apical junction plane while following the local disc curvature. *hid*$^{\Delta GFP}$ pattern measurements were done after fixation and GFP immunostaining and maximum z projection. The mean GFP intensity was measured in each compartment (defined with DSRF staining) and normalised by the mean GFP intensity of the full wing pouch.

QMARCM and mitotic clones experiments

Wandering larvae were collected 48 hours after clone induction following a 37°C heat-shock of 8 or 10 minutes (Table 2). Analysis of twin clones was performed on local projections of the wing discs after fixation and staining. Only discs with sufficiently sparse distribution of clones were used (to assign twins unambiguously). To extract clone position and size, each mitotic recombination figure (twin spot or single clone) was manually outlined on FIJI and then automatically segmented by applying a Gaussian blur followed by an automated thresholding (Intermode white method). The centroid of each mitotic recombination figure was obtained by summing the centres of each individual patch of cells composing the twin spot, ponderated by their relative area compared to the total area of the twin clone. Thus, the centroid of each mitotic recombination figure was given by the following formula:

$$Centroid\ (x,y)_{mitotic\ figure} = \sum_{clone\ i} (Centroid\ (x,y)_{\ patch\ i}).\frac{Area_{patch\ i}}{Total\ Area\ twin\ clone}$$

Averaged clone surface was estimated through the segmented surface of GFP or RFP clones (using the local projection around the apical plane of cells). Estimation of the clone size in cell number was obtained a posteriori by segmenting (using Tissue

analyser[71]) 3 wing discs stained with E-cad (Figure 3suppA') and DSRF to position landmarks, and by estimating the averaged apical cell area for each compartment. The 3 wing discs segmented for apical cell area shown a very congruent pattern (Figure 3suppA), thus allowing to pool the data from the 3 discs (Figure supp3 B). The average surface of clone for each compartment was then divided by the local averaged cell size to obtain an estimation of cell number per clone and to correct for effects driven by inhomogeneity of cell apical size throughout the disc.

For mitotic clones (H99 and WT sibling clones, ubi-GFP and arm-β-gal WT neutral mitotic clones), E-cad and phalloidin signals were used to project locally the β-gal signal (the absence of LacZ marking the H99 allele) using the local z-projection Fiji plugin [70] and combined with DSRF staining. The same procedure was applied to GFP and β-gal for neutral mitotic clones, except that the projection was performed around the nucleus plane. A 3D gaussian blur filter was applied on the β-gal and GFP signal (1px width in X,Y,Z). For H99 mitotic clones, homozygous mutant (no β-gal signal) and WT siblings (2 copies of β-gal) were recognised manually, and their contours drawn by hands on Fiji. The same procedure was applied to neutral mitotic clones (comparing clones with 2 copies of β-gal without GPF, and clones with two copies of GFP without β-gal). We only used discs with sufficiently sparse clones and proper β-gal/GFP signal and counted single clone only when there was no ambiguity. Twin clone localisation was then assigned using the centroid estimation described above.

Spatial maps of wing discs (twin clones and GC3Ai).

Positions of 36 landmarks were manually set on Z projections of wing discs using FIJI. Landmarks were positioned according to the pattern of DSRF revealed by immunostaining, along the veins, margin and folds of the wing pouch (**Figure 1supp A,B**). Two methods were used to characterise a spatial map of the tissue based on landmarks position. For the first one, landmarks were geometrically aligned within each genotype using the General Procrustes Analysis (GPA) [72] as implemented in R geomorph package [73]. GPA translates the set of landmarks of each wing disc to the same origin, scales them to size, and rotates them until the coordinates of corresponding points align as closely as possible. GPA allows to superimpose as closely as possible several wing discs, thus allowing superimposition of the signal from

many individuals (**Figure 1F, Figure 1supp,H,J,M,P,R**). For the second mapping method, 14 additional landmarks were added (landmarks 37 to 50) at the centre of segments defined by other landmarks (for example landmark 37 was set as the centre of the segment defined by landmarks 21 and 22, **Figure 1suppC**). The resulting 50 landmarks were thus used to define polygons dividing the wing disc tissue into 40 compartments (**Figure 1suppC**). With this later approach, clones and apoptotic bodies (defined by GC3Ai or cleaved DCP-1 figures) were assigned to a compartment according to the coordinates of the centre of mass of the clone/apoptotic body. In order to account for uncertainty in clone/apoptotic body localisation (e.g., because of clone movement between the time of induction and imaging), as well as for uncertainty in landmark positioning (e.g., because of immunostaining variability or user error), clone assignment included consideration of an error margin. We used the *st_buffer* function implemented in the *sf* package of R software to add an error margin at a distance of 11.8 µm (40 pixels) around compartment margins (**Fig. 1suppD**). As a result, buffered boundaries of neighbour compartments overlap within each other and a given position in the tissue could be assigned to belong to more than one compartment. This results in a smoothing of the spatial map allowing to account for uncertainty in cells and landmarks positions.

To analyse the spatial pattern of GC3Ai in discs at 72 h AEL, the anti DSRF staining could not be used to draw the landmarks because at this stage the DSRF patterning is not yet established. Instead we stained the wing discs for Ptc and Wg to detect AP and DV compartment and subdivide the wing disc in 4 quadrants (Anterior-Dorsal; Anterior-Ventral; Posterior-Dorsal; Posterior-Ventral).

Adult wing shape and size analyses

Crosses were done by placing 50-100 couples in egg laying cages with juice-agar plates kept at 25 °C. Freshly hatched larva from the agar plates were transferred to *Drosophila* vials with fly food as described above at a density of 30 individuals / vial, and grown at 18 °C, 25 °C or 29 °C until emergence of adults. Flies were collected and stored in ethanol 70 % at room temperature until dissection. Only left wings from females were taken, and mounted dorsal side up on a glass slide in a solution of 1:1 ethanol 80% and lactic acid 90%. Imaging was carried out on a ZEISS Discovery V8 stereomicroscope using a ZEISS Axiocam ICc 5 camera. All wings were imaged in the

same orientation and with the same imaging parameters. For the experiments using Gal80ts (**Figures 4** and **4supp**), flies were crossed in cages supplied with agar petri dishes and allowed to lay eggs for 6 to 12 h. Freshly hatched larva were transferred to regular vials at a density of 30 individuals / tube, and placed at 18 °C or 29 °C. Once arrived at the wandering larval stage, individuals where switched temperature (from 18 °C to 29 °C and vice-versa). Upon hatching, flies were collected for wing dissection.

Wing measurements were done using a semi-automated procedure for estimating the positions of 12 landmarks and 37 semi-landmarks along the wing outline and veins (**Figure 4suppA**). This was done using Wings4 software [52, 53] which fits a B-spline model to the wing from which the coordinates of landmarks and semi-landmarks are extracted. Wings4 outputs were examined using CPR software[53] which allows to screen for outliers and to generate a consolidated dataset of landmarks and wing areas.

Landmarks data were geometrically aligned within each experiment using the General Procrustes Analysis (GPA)[72] as implemented in R geomorph package[73]. GPA translates all wing images to the same origin, scales them to unit-centroid size (centroid size is a measure of specimen size computed as the square root of the sum of squared distances of all the landmarks from the specimen's centroid) and rotates them until the coordinates of corresponding points align as closely as possible. Differences in landmarks coordinates resulting from the GPA represent shape differences between wings. Wing shape of each individual is characterised by the value of 96 variables, coming from the Procrustes transformation of x and y coordinates of the 48 landmarks and semi-landmarks. To reduce dimensionality of the data, wing shape variation was analysed by Principal Components Analysis as implemented in the function *plotTangentSpace* (now deprecated and replaced by *gm.prcomp*) of the R *geomorph* package. Visualisation of the wing shape variation among the principal component axes was done by comparing wing shape of the individual presenting the lowest value along the axis, with the individual presenting the highest value. To enable visualisation of local growth differences in the adult wing upon apoptosis inhibition, we used the program Lory[74] to show one pattern of relative expansion or contraction that can transform mean shape of control genotype into mean shape of genotypes where apoptosis was inhibited.

Live imaging of pupal wing

Pupa were collected at early fluid stage and kept at 29°C for 7 h, resulting in pupa aged of ~15 h APF (after pupal formation). Pupal wings were prepared for live imaging as described in [75]. Briefly, pupa were glued on their lateral side on a support made of three layers of tape (one layer of single-side tape, a second layer of double-side tape, and a third layer of single-side tape), and a window was opened using a pair of fine scissors (Fine Science Tools) in the pupal case to expose the pupal wing tissue. The wing was covered with halocarbon 10S oil, and the tape with the pupa on it was mounted on a glass bottom dish of 1,5 µm thickness (Miltenyi Biotec). Imaging was done on a confocal spinning disc microscope (Gataca systems, Metamorph software) with a multi-immersion 20X objective with oil (N.A. 0.75). The dorsal epithelial layer of the wing was scanned on a mosaic of two (x,y) tiles, and Z-stacks of 50 µm (20 slices of 2.5 µm), every 15 min at room temperature (~ 22 °C). Z projections were done using the Fiji LocalZProjector using E-cad plane as a reference [70].

Estimation of clone size differences in an exponential growth regime

The aim of this analysis is to predict spatial differences of clone size under an exponential growth regime given the estimated spatial differences of apoptosis rate based on the twin-clone experimental assays. For the sake of simplicity, we assume that division rate and apoptosis rate are constant over time.

Estimation of the clone extinction probability

Upon recombination, two daughter cells of different colours are generated and continue to grow, divide and die. After a given time T (time of observation), there are four possible outcomes: we can recover the two daughter clones, a single colour clone, green or red (the other clone died before time T), and finally both clones disappeared before time T (which cannot be measured experimentally). For this estimation, we assumed that both lineages (green and red) have the same proliferation and death rates.

$n(t)$ is the size (number of cells) of a clone at the time t, and it obeys to? a stochastic process that follows the same probability function for every clone. For every clone, we have $n(0) = 1$. The probability of clone disappearance before time t. *i.e.* the extinction probability, $p_0(t)$ is defined as

$$p_0(t) = P(n(t) = 0).$$

Experimental data gives access to the number of single clones N_s and to the number of twin clones N_d that we observe at the time T. From this, we can estimate the probability of extinction at the observation time T, $p_0 = p_0(T)$.

The expected number of single clones is $N_s = 2p_0(1 - p_0)$

The expected number of twin clones is $N_d = (1 - p_0)^2$

which gives the estimator of p_0,

(1) $\hat{p_0} = \frac{q}{2-q}$

where $q = \frac{N_s}{N_s+N_d}$

Estimation of the clone size and relationship with apoptosis and proliferation rate

Let $\mu(t)$ be mean value of $n(t)$, clone size in number of cell at time *t*. In theory,

$$\mu(t) = p_0(t) \cdot 0 + p_1(t) \cdot 1 + \cdots + p_i(t) \cdot i + \cdots,$$

where $p_i(t)$ is a probability to observe a clone of size i at the given time t, or $p_i(t) = P(n(t) = i)$ and $\sum p_i(t) = 1$ for all t. In order to estimate $\mu(t)$ from the observations we use:

$$\hat{\mu} = \frac{k_0}{N} \cdot 0 + \frac{k_1}{N} \cdot 1 + \cdots + \frac{k_i}{N} \cdot i + \cdots,$$

where N is a total number of clones (including clones of size "0"), k_i is a number of clones of size i, and $\sum k_i = N$.

However, since we cannot observe clones of size 0 we cannot measure k_0 nor N. We therefore use $p_0 = \frac{k_0}{N}$ (the probability of clone extinction, see above), and the total number of observed clones $N_{obs} = N - k_0$. From these two we can estimate $N = \frac{N_{obs}}{1-p_0}$. Hence, we estimate μ with

(2) $\hat{\mu} = (1 - \hat{p_0}) \left(\frac{k_1}{N_{obs}} \cdot 1 + \cdots + \frac{k_i}{N_{obs}} \cdot i + \cdots \right).$

Each clone observed is a result of a stochastic birth-death process, that is fully described by its death rate, a, which is a probability of an individual cell to die per unit time and its birth rate, b, which is a probability of an individual cell to divide per unit time. While the size of the clone at the given time, $n(t)$, is a stochastic process, the mean size $\mu(t)$ can be approximated by a deterministic process and is given by the following exponential function:

(3) $$\mu(t) = e^{(b-a)t}$$

Furthermore, the probability to be extinct at the time t ($n(t) = 0$) can be expressed as follows [76]:

(4) $$p_0(t) = \frac{a - ae^{-(b-a)t}}{b - ae^{-(b-a)t}}$$

Estimating the apoptosis and proliferation rates for each compartment.

From the twin clone experimental data, we retrieve for each compartment the proportion of single clone occurrence (**Figure 2C**) and the averaged clone size (**Figure 3A**) which, together with *(1), allows us to* estimate p_0, and μ for each of the 40 compartments of the wing disc. These estimates can then be used to estimate parameters a and b (apoptosis and division rate). For the fixed t, based on *(3)* and *(4)* we have:

(5) $$b = \frac{\ln(\mu)}{t} + a$$

and

(6) $$p_0 = \frac{a - \frac{a}{\mu}}{b - \frac{a}{\mu}}$$

Hence

(7) $$a = \frac{\ln(\mu)}{t\left[\frac{1}{\mu} + \frac{\mu - 1}{\mu p_0} - 1\right]}$$

Estimating the expected differences of clone size between compartments assuming constant proliferation rate

We use the fixed value of a birth rate, $b = 0.0657$ (average of the estimated *b* from *(5)*), as a fixed value for every compartment. We look for a death rates a for each compartment using the expression for $p_0(a)$ *(4)*. To the best of our knowledge it is not possible to express explicitly a from the given formulation, so we use numerical approach to calculate it. We plot function of p_0 as $p_0(a)$ and look for the point of intersection with the measured value $\hat{p}_0$. In this way we estimate value of a. Then we use a and the fixed value of b to predict μ *(6)*, that we then compared with the estimated value $\hat{\mu}$ from the experimental data *(2)* correcting for the non-observable disappeared clones (see **Figure 3B**). We overall found a good correlation between the estimated clone size and the prediction, (correlation coefficient $\rho = 0.6$, **Figure 3D**) suggesting that the spatial differences in apoptosis are to a good approximation sufficient to explain the spatial differences in average clone size.

Statistics

Data were not analysed blindly. No specific method was used to predetermine the number of samples. The definition of n and the number of samples is given in each figure and associated legend. Error bars are standard error of the mean (s.e.m.) or confidence interval 95%. Test for spatial autocorrelations in apoptosis patterns were conducted using Moran's statistics implemented in the *moran.mc* function from the *spdep* R package[77]. This tests for spatial clustering of apoptosis levels, by testing the hypothesis that the levels of apoptosis are randomly distributed across the 40 compartments, versus the hypothesis that the level of apoptosis of a given compartment is correlated with the levels of the neighbouring compartments. Tests for spatial correlation across compartments between log transformed GC3Ai levels and % of single clones occurrences were done using the function *wtd.cor* from *weights* R package (v. 1.0.4), which produces a Pearsons correlation test and uses weights for calculation of the correlations. In this case, we weighted the values for the % of single clones by the number of mitotic events over which the percentage was estimated within each compartment, thus giving higher weights to the compartments for which percentages were estimated over a large number of events. Bootstrapping analysis was used to assess the distribution of differences between Hid-dsRNA and LacZ adult wing size at different temperatures upon larval and pupal induction at 29°C (**Figure 5A**). 50 random resamplings of each dataset was performed and used to look at the percentage of variation of the difference obtained for each condition between the lacZ

and Hid-dsRNA flies. We then assessed the overlap of the distribution and confirmed that the difference between LacZ and Hid-dsRNA at 18° (control) is similar to the difference between LacZ and Hid-dsRNA induction during pupal stage (18°C-29°C), while the differences were higher than the control for all the other conditions.

References

1. Lecuit, T., and Le Goff, L. (2007). Orchestrating size and shape during morphogenesis. Nature *450*, 189-192.
2. Fuchs, Y., and Steller, H. (2011). Programmed cell death in animal development and disease. Cell *147*, 742-758.
3. Toyama, Y., Peralta, X.G., Wells, A.R., Kiehart, D.P., and Edwards, G.S. (2008). Apoptotic force and tissue dynamics during Drosophila embryogenesis. Science *321*, 1683-1686.
4. Monier, B., Gettings, M., Gay, G., Mangeat, T., Schott, S., Guarner, A., and Suzanne, M. (2015). Apico-basal forces exerted by apoptotic cells drive epithelium folding. Nature *518*, 245-248.
5. Roellig, D., Theis, S., Proag, A., Allio, G., Benazeraf, B., Gros, J., and Suzanne, M. (2022). Force-generating apoptotic cells orchestrate avian neural tube bending. Dev Cell.
6. Claveria, C., and Torres, M. (2016). Cell Competition: Mechanisms and Physiological Roles. Annu Rev Cell Dev Biol *32*, 411-439.
7. Adachi-Yamada, T., Fujimura-Kamada, K., Nishida, Y., and Matsumoto, K. (1999). Distortion of proximodistal information causes JNK-dependent apoptosis in Drosophila wing. Nature *400*, 166-169.
8. Adachi-Yamada, T., and O'Connor, M.B. (2002). Morphogenetic apoptosis: a mechanism for correcting discontinuities in morphogen gradients. Dev Biol *251*, 74-90.
9. Gibson, M.C., and Perrimon, N. (2005). Extrusion and death of DPP/BMP-compromised epithelial cells in the developing Drosophila wing. Science *307*, 1785-1789.
10. Shen, J., and Dahmann, C. (2005). Extrusion of cells with inappropriate Dpp signaling from Drosophila wing disc epithelia. Science *307*, 1789-1790.
11. Bielmeier, C., Alt, S., Weichselberger, V., La Fortezza, M., Harz, H., Julicher, F., Salbreux, G., and Classen, A.K. (2016). Interface Contractility between Differently Fated Cells Drives Cell Elimination and Cyst Formation. Curr Biol *26*, 563-574.
12. Merino, M.M., Seum, C., Dubois, M., and Gonzalez-Gaitan, M. (2022). A role for Flower and cell death in controlling morphogen gradient scaling. Nat Cell Biol.
13. Boulan, L., and Leopold, P. (2021). What determines organ size during development and regeneration? Development *148*.
14. Vollmer, J., Casares, F., and Iber, D. (2017). Growth and size control during development. Open Biol *7*.
15. Hariharan, I.K. (2015). Organ Size Control: Lessons from Drosophila. Dev Cell *34*, 255-265.
16. Wartlick, O., Mumcu, P., Kicheva, A., Bittig, T., Seum, C., Julicher, F., and Gonzalez-Gaitan, M. (2011). Dynamics of Dpp signaling and proliferation control. Science *331*, 1154-1159.
17. Harmansa, S., Hamaratoglu, F., Affolter, M., and Caussinus, E. (2015). Dpp spreading is required for medial but not for lateral wing disc growth. Nature *527*, 317-322.
18. Strassburger, K., Lutz, M., Muller, S., and Teleman, A.A. (2021). Ecdysone regulates Drosophila wing disc size via a TORC1 dependent mechanism. Nat Commun *12*, 6684.
19. Akiyama, T., and Gibson, M.C. (2015). Decapentaplegic and growth control in the developing Drosophila wing. Nature *527*, 375-378.
20. Gerhold, A.R., Richter, D.J., Yu, A.S., and Hariharan, I.K. (2011). Identification and characterization of genes required for compensatory growth in Drosophila. Genetics *189*, 1309-1326.

21. Hecht, S., Perez-Mockus, G., Schienstock, D., Recasens-Alvarez, C., Merino-Aceituno, S., Smith, M., Salbreux, G., Degond, P., and Vincent, J.P. (2022). Mechanical constraints to cell-cycle progression in a pseudostratified epithelium. Curr Biol *32*, 2076-2083 e2072.
22. Voss, A.K., and Strasser, A. (2020). The essentials of developmental apoptosis. F1000Res *9*.
23. Milán, M., Campuzano, S., and García-Bellido, A. (1997). Developmental parameters of cell death in the wing disc of Drosophila. Proceedings of the National Academy of Sciences of the United States of America *94*, 5691-5696.
24. Mailleux, A.A., Overholtzer, M., Schmelzle, T., Bouillet, P., Strasser, A., and Brugge, J.S. (2007). BIM regulates apoptosis during mammary ductal morphogenesis, and its absence reveals alternative cell death mechanisms. Dev Cell *12*, 221-234.
25. Eder, D., Aegerter, C., and Basler, K. (2017). Forces controlling organ growth and size. Mech Dev *144*, 53-61.
26. Aigouy, B., Farhadifar, R., Staple, D.B., Sagner, A., Roper, J.C., Julicher, F., and Eaton, S. (2010). Cell flow reorients the axis of planar polarity in the wing epithelium of Drosophila. Cell *142*, 773-786.
27. Etournay, R., Popovic, M., Merkel, M., Nandi, A., Blasse, C., Aigouy, B., Brandl, H., Myers, G., Salbreux, G., Julicher, F., et al. (2015). Interplay of cell dynamics and epithelial tension during morphogenesis of the Drosophila pupal wing. Elife *4*, e07090.
28. Romanova-Michaelides, M., Hadjivasiliou, Z., Aguilar-Hidalgo, D., Basagiannis, D., Seum, C., Dubois, M., Julicher, F., and Gonzalez-Gaitan, M. (2022). Morphogen gradient scaling by recycling of intracellular Dpp. Nature *602*, 287-293.
29. Matamoro-Vidal, A., Salazar-Ciudad, I., and Houle, D. (2015). Making quantitative morphological variation from basic developmental processes: Where are we? The case of the Drosophila wing. Dev Dyn *244*, 1058-1073.
30. Tripathi, B.K., and Irvine, K.D. (2022). The wing imaginal disc. Genetics.
31. Martin, F.A., Herrera, S.C., and Morata, G. (2009). Cell competition, growth and size control in the Drosophila wing imaginal disc. Development *136*, 3747-3756.
32. Garcia-Bellido, A., and Merriam, J.R. (1971). Parameters of the wing imaginal disc development of Drosophila melanogaster. Dev Biol *24*, 61-87.
33. Diaz de la Loza, M.C., and Thompson, B.J. (2017). Forces shaping the Drosophila wing. Mechanisms of Development *144*, 23-32.
34. Srivastava, A., Pastor-Pareja, J.C., Igaki, T., Pagliarini, R., and Xu, T. (2007). Basement membrane remodeling is essential for Drosophila disc eversion and tumor invasion. Proceedings of the National Academy of Sciences of the United States of America *104*, 2721-2726.
35. Sun, T., Song, Y., Teng, D., Chen, Y., Dai, J., Ma, M., Zhang, W., and Pastor-Pareja, J.C. (2021). Atypical laminin spots and pull-generated microtubule-actin projections mediate Drosophila wing adhesion. Cell Rep *36*, 109667.
36. Ray, R.P., Matamoro-Vidal, A., Ribeiro, P.S., Tapon, N., Houle, D., Salazar-Ciudad, I., and Thompson, B.J. (2015). Patterned Anchorage to the Apical Extracellular Matrix Defines Tissue Shape in the Developing Appendages of Drosophila. Dev Cell *34*, 310-322.
37. Tsuboi, A., Fujimoto, K., and Kondo, T. (2023). Spatio-temporal remodeling of extracellular matrix orients epithelial sheet folding. bioRxiv, 2023.2001.2013.523870.
38. Peabody, N.C., and White, B.H. (2013). Eclosion gates progression of the adult ecdysis sequence of Drosophila. J Exp Biol *216*, 4395-4402.
39. Abouchar, L., Petkova, M.D., Steinhardt, C.R., and Gregor, T. (2014). Fly wing vein patterns have spatial reproducibility of a single cell. J R Soc Interface *11*, 20140443.
40. Guirao, B., Rigaud, S.U., Bosveld, F., Bailles, A., Lopez-Gay, J., Ishihara, S., Sugimura, K., Graner, F., and Bellaiche, Y. (2015). Unified quantitative characterization of epithelial tissue development. Elife *4*.
41. de la Cova, C., Abril, M., Bellosta, P., Gallant, P., and Johnston, L.A. (2004). Drosophila myc regulates organ size by inducing cell competition. Cell *117*, 107-116.

42. Levayer, R., and Moreno, E. (2013). Mechanisms of cell competition: themes and variations. J Cell Biol *200*, 689-698.
43. Morata, G., and Ripoll, P. (1975). Minutes: mutants of drosophila autonomously affecting cell division rate. Dev Biol *42*, 211-221.
44. Shinoda, N., Hanawa, N., Chihara, T., Koto, A., and Miura, M. (2019). Dronc-independent basal executioner caspase activity sustains Drosophila imaginal tissue growth. Proceedings of the National Academy of Sciences of the United States of America *116*, 20539-20544.
45. Schott, S., Ambrosini, A., Barbaste, A., Benassayag, C., Gracia, M., Proag, A., Rayer, M., Monier, B., and Suzanne, M. (2017). A fluorescent toolkit for spatiotemporal tracking of apoptotic cells in living Drosophila tissues. Development *144*, 3840-3846.
46. Rodriguez, A., Oliver, H., Zou, H., Chen, P., Wang, X., and Abrams, J.M. (1999). Dark is a Drosophila homologue of Apaf-1/CED-4 and functions in an evolutionarily conserved death pathway. Nat Cell Biol *1*, 272-279.
47. Potter, C.J., Tasic, B., Russler, E.V., Liang, L., and Luo, L. (2010). The Q system: a repressible binary system for transgene expression, lineage tracing, and mosaic analysis. Cell *141*, 536-548.
48. Legoff, L., Rouault, H., and Lecuit, T. (2013). A global pattern of mechanical stress polarizes cell divisions and cell shape in the growing Drosophila wing disc. Development *140*, 4051-4059.
49. Gibson, M.C., Patel, A.B., Nagpal, R., and Perrimon, N. (2006). The emergence of geometric order in proliferating metazoan epithelia. Nature *442*, 1038-1041.
50. Rezaval, C., Werbajh, S., and Ceriani, M.F. (2007). Neuronal death in Drosophila triggered by GAL4 accumulation. Eur J Neurosci *25*, 683-694.
51. White, K., Grether, M.E., Abrams, J.M., Young, L., Farrell, K., and Steller, H. (1994). Genetic control of programmed cell death in Drosophila. Science *264*, 677-683.
52. Houle, D., Mezey, J., Galpern, P., and Carter, A. (2003). Automated measurement of drosophila wings. Bmc Evolutionary Biology *3*.
53. Houle, D., Van der Linde, K., and Marquez, E. (2014). Wings: Automated Capture of Drosophila Wing Shape v. 4.0.
54. Siegrist, S.E., Haque, N.S., Chen, C.H., Hay, B.A., and Hariharan, I.K. (2010). Inactivation of both Foxo and reaper promotes long-term adult neurogenesis in Drosophila. Curr Biol *20*, 643-648.
55. Leevers, S.J., Weinkove, D., MacDougall, L.K., Hafen, E., and Waterfield, M.D. (1996). The Drosophila phosphoinositide 3-kinase Dp110 promotes cell growth. EMBO J *15*, 6584-6594.
56. Blanco-Obregon, D., El Marzkioui, K., Brutscher, F., Kapoor, V., Valzania, L., Andersen, D.S., Colombani, J., Narasimha, S., McCusker, D., Leopold, P., et al. (2022). A Dilp8-dependent time window ensures tissue size adjustment in Drosophila. Nat Commun *13*, 5629.
57. McDonald, J.M.C., Ghosh, S.M., Gascoigne, S.J.L., and Shingleton, A.W. (2018). Plasticity Through Canalization: The Contrasting Effect of Temperature on Trait Size and Growth in Drosophila. Front Cell Dev Biol *6*, 156.
58. Diwanji, N., and Bergmann, A. (2019). Two Sides of the Same Coin - Compensatory Proliferation in Regeneration and Cancer. Adv Exp Med Biol *1167*, 65-85.
59. Haynie, J.L., and Bryant, P.J. (1977). The effects of X-rays on the proliferation dynamics of cells in the imaginal wing disc ofDrosophila melanogaster. Wilehm Roux Arch Dev Biol *183*, 85-100.
60. Huh, J.R., Guo, M., and Hay, B.A. (2004). Compensatory proliferation induced by cell death in the Drosophila wing disc requires activity of the apical cell death caspase Dronc in a nonapoptotic role. Curr Biol *14*, 1262-1266.
61. Perez-Garijo, A., Shlevkov, E., and Morata, G. (2009). The role of Dpp and Wg in compensatory proliferation and in the formation of hyperplastic overgrowths caused by apoptotic cells in the Drosophila wing disc. Development *136*, 1169-1177.
62. Ankawa, R., Goldberger, N., Yosefzon, Y., Koren, E., Yusupova, M., Rosner, D., Feldman, A., Baror-Sebban, S., Buganim, Y., Simon, D.J., et al. (2021). Apoptotic cells represent a dynamic stem cell niche governing proliferation and tissue regeneration. Dev Cell *56*, 1900-1916 e1905.

63. Kawaue, T., Yow, I., Pan, Y., Le, A.P., Lou, Y., Loberas, M., Shagirov, M., Teng, X., Prost, J., Hiraiwa, T., et al. (2023). Inhomogeneous mechanotransduction defines the spatial pattern of apoptosis-induced compensatory proliferation. Dev Cell *58*, 267-277 e265.
64. Merino, M.M., Rhiner, C., Lopez-Gay, J.M., Buechel, D., Hauert, B., and Moreno, E. (2015). Elimination of unfit cells maintains tissue health and prolongs lifespan. Cell *160*, 461-476.
65. Houle, D., Bolstad, G.H., van der Linde, K., and Hansen, T.F. (2017). Mutation predicts 40 million years of fly wing evolution. Nature *548*, 447-450.
66. Crossman, S.H., Streichan, S.J., and Vincent, J.P. (2018). EGFR signaling coordinates patterning with cell survival during Drosophila epidermal development. PLoS Biol *16*, e3000027.
67. Pinheiro, D., Hannezo, E., Herszterg, S., Bosveld, F., Gaugue, I., Balakireva, M., Wang, Z., Cristo, I., Rigaud, S.U., Markova, O., et al. (2017). Transmission of cytokinesis forces via E-cadherin dilution and actomyosin flows. Nature *545*, 103-107.
68. Chimata, A.V., Deshpande, P., Mehta, A.S., and Singh, A. (2022). Protocol to study cell death using TUNEL assay in Drosophila imaginal discs. STAR Protoc *3*, 101140.
69. Schindelin, J., Arganda-Carreras, I., Frise, E., Kaynig, V., Longair, M., Pietzsch, T., Preibisch, S., Rueden, C., Saalfeld, S., Schmid, B., et al. (2012). Fiji: an open-source platform for biological-image analysis. Nat Methods *9*, 676-682.
70. Herbert, S., Valon, L., Mancini, L., Dray, N., Caldarelli, P., Gros, J., Esposito, E., Shorte, S.L., Bally-Cuif, L., Aulner, N., et al. (2021). LocalZProjector and DeProj: a toolbox for local 2D projection and accurate morphometrics of large 3D microscopy images. BMC Biol *19*, 136.
71. Etournay, R., Merkel, M., Popovic, M., Brandl, H., Dye, N.A., Aigouy, B., Salbreux, G., Eaton, S., and Julicher, F. (2016). TissueMiner: A multiscale analysis toolkit to quantify how cellular processes create tissue dynamics. Elife *5*.
72. Rohlf, F.J., and Slice, D. (1990). Extensions of the Procrustes Method for the Optimal Superimposition of Landmarks. Systematic Zoology *39*, 40-59.
73. Adams, D.C., and Otarola-Castillo, E. (2013). geomorph: an r package for the collection and analysis of geometric morphometric shape data. Methods in Ecology and Evolution *4*, 393-399.
74. Marquez, E.J., Cabeen, R., Woods, R.P., and Houle, D. (2012). The Measurement of Local Variation in Shape. Evol Biol *39*, 419-439.
75. Classen, A.K., Aigouy, B., Giangrande, A., and Eaton, S. (2008). Imaging Drosophila pupal wing morphogenesis. Methods Mol Biol *420*, 265-275.
76. van Kampen, N.G. (2007). STOCHASTIC PROCESSES IN PHYSICS AND CHEMISTRY Third edition PREFACE TO THE THIRD EDITION. North-Holl Pers Libr, Xi-Xi.
77. Bivand, R.S., and Wong, D.W.S. (2018). Comparing implementations of global and local indicators of spatial association TEST. *27(3)*, 716-748.

Figure 1

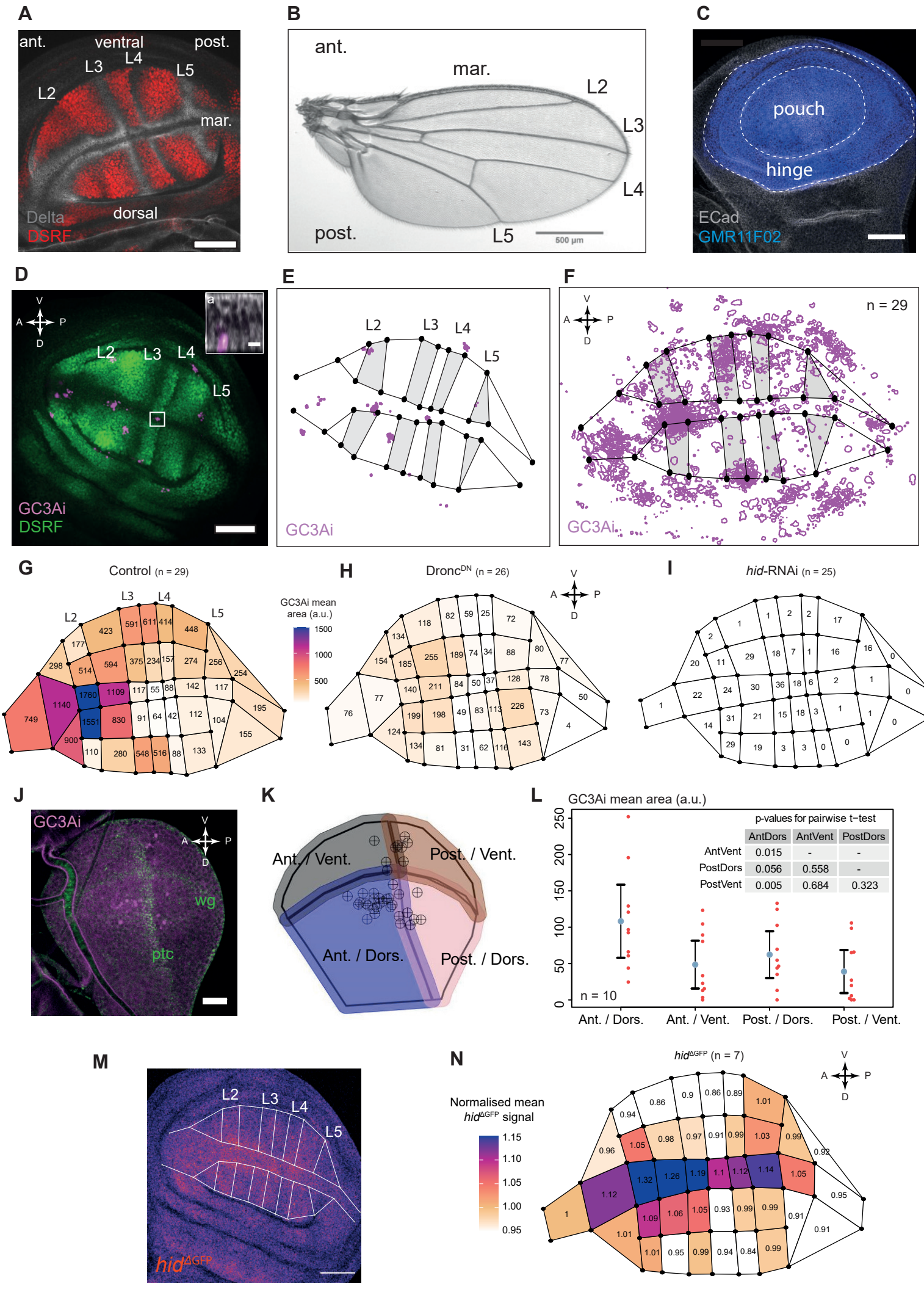
A
ant.
ventral
post.
L3
L4
L5
L2
mar.
Delta
DSRF
dorsal
B
ant.
mar.
L2
L3
L4
post.
L5
500 µm
C
pouch
hinge
ECad
GMR11F02
D
V
A
P
D
a
L2
L3
L4
L5
GC3Ai
DSRF
E
L2
L3
L4
L5
GC3Ai
F
n = 29
GC3Ai
G
Control (n = 29)
GC3Ai mean area (a.u.)
1500
1000
500
H
Dronc^DN (n = 26)
I
hid-RNAi (n = 25)
J
GC3Ai
wg
ptc
K
Ant. / Vent.
Post. / Vent.
Ant. / Dors.
Post. / Dors.
L
GC3Ai mean area (a.u.)
p-values for pairwise t−test
AntDors AntVent PostDors
AntVent 0.015 - -
PostDors 0.056 0.558 -
PostVent 0.005 0.684 0.323
n = 10
Ant. / Dors.
Ant. / Vent.
Post. / Dors.
Post. / Vent.
M
L2
L3
L4
L5
hidΔGFP
N
hidΔGFP (n = 7)
Normalised mean hidΔGFP signal
1.15
1.10
1.05
1.00
0.95

Figure 1: Apoptosis is spatially biased in the developing wing tissue.

A: Wing disc at ~ 96 h after egg laying (AEL) showing veins (L2 to L5), interveins (red), dorsal, ventral, margin (mar.), anterior (ant.) and posterior (post.) territories. Red: anti-DSRF immunostaining. Grey: anti-Delta immunostaining. Orientation is the same for all wing discs images and schemes of this article, with the anterior compartment leftwards, and the dorsal compartment downwards. **B:** Female adult wing on dorsal view, with longitudinal veins (L2 to L5), margin (mar.), anterior (ant.) and posterior (post.) territories. **C:** Wing disc at ~ 96 h AEL showing the GMR11F02-GAL4 expression domain (blue). Gray: anti E-Cadherin immunostaining. **D:** z-projection of a wing disc showing caspase-3 activity using the GC3Ai reporter (magenta) expressed under the control of GMR11F02-GAL4 at ~ 96 h AEL. The inset is an orthogonal view of the white square, showing that the GC3Ai signal (magenta) points to apoptotic bodies located basally in the epithelium. a: apical. Grey: E-Cadherin. Inset scale bar: 5 µm. **E:** Segmentation output from the disc in **D**, showing the DSRF pattern and the GC3Ai segmented signal (magenta). Veins regions are grey. **F:** Superimposition of the segmentation data from 29 discs scaled, rotated and aligned using the General Procrustes Analysis (GPA), showing a spatially heterogeneous signal for GC3Ai (magenta). The map shown for vein / intervein territories is the average map from the 29 discs. **G-I:** Heat-maps showing the average GC3Ai positive area on each of the 40 compartments of the wing disc for the *control* (**G**, n = 29), *Dronc*^{DN} (**H**, n = 26), *hid-RNAi* (**I**, n = 25) genotypes. Numbers within each compartment show the average value for GC3Ai positive area (arbitrary units). These values are also shown as a colour coded heat-map which has the same scale for three maps shown in G-I. **J:** Visualisation of caspase-3 activity using the GC3Ai reporter (magenta) expressed under the control of GMR11F02-GAL4 at ~ 72 h AEL. The wing disc is divided into four quadrants (Anterior-Dorsal; Anterior-Ventral; Posterior-Dorsal; Posterior-Ventral) using the immunostaining anti Wingless (wg) and antiPatched (ptc) marking compartment boundaries. **K:** Segmentation of the disc shown in **J**. The circled black crosses denote the centroids of the segmented GC3Ai signal. The black line was manually drawn using anti-Wingless and anti-Patched immunostainings to delineate the four quadrants, which are coloured. In order to account for uncertainty in centroid location and manual drawing of the contours, an overlap between the quadrants was allowed. **L:** Mean GC3Ai positive area for 10 discs at ~ 72 h AEL. One red dot represents one disc, blue circles are means and error bars are 95 % confidence intervals. The inset shows the p-values for all pairwise t-tests between quadrants. **M:** Pattern of *hid*$^{\Delta GFP}$(KI) on a single wing disc (LUT fire, Gaussian blur 0.75). White lines denote the vein/intervein territories extracted from the anti-DSRF immunostaining (not shown). **N:** Heat-map showing the mean *hid*$^{\Delta GFP}$ signal on each of the 40 compartments over n = 17 discs. To allow comparison of intensities among discs, the GFP signal intensity was normalised within each disc (i.e., within each disc, the value of each pixel was divided by the mean signal intensity over all the pixels of the disc). All scale bars are 50 µm length excepted in **B**, 500 µm, and in **J**, 25 µm.

Supplementary figure 1

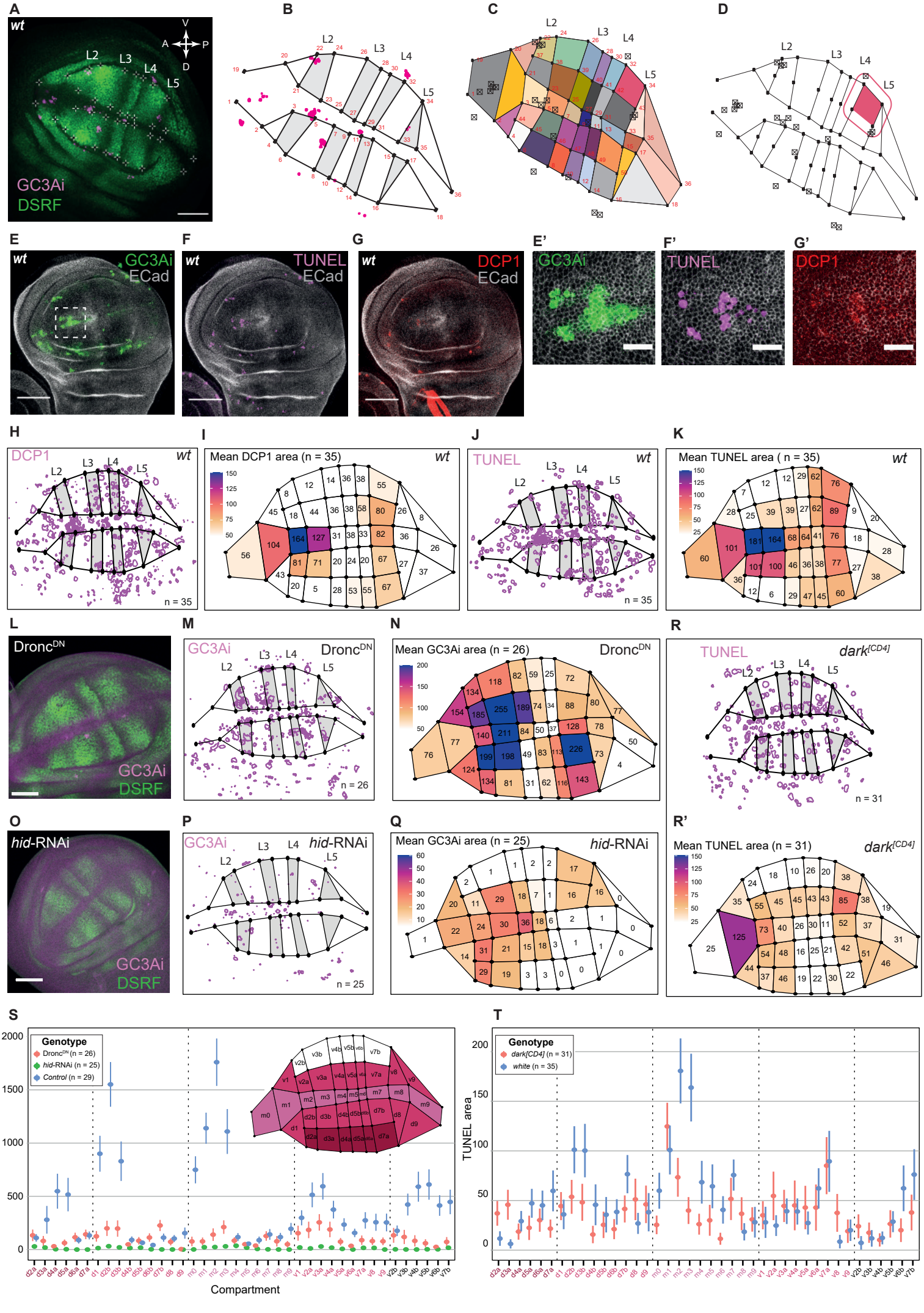

Supplementary figure 1 (related to Figure 1)

A: Wing disc from **Fig. 1-A** showing the 36 landmarks (white crosses) that were manually positioned at the intersections between veins (L2 to L5), folds and margins of the tissue, visible thanks to DSRF (green). **B:** Map of the wing disc shown in **A**, drawn from the landmark positions (black dots, numbered 1 to 36), and showing the segmented GC3Ai signal (magenta). Vein regions are in grey and intervein/margin regions in white. **C:** Division of the wing disc map shown in **B** into 40 compartments based on polygons (plain colours) defined with the landmarks. To this aim, 14 additional landmarks (numbered 37 to 50) were added at the middle of segments made by previously defined landmarks (see **Methods**). Boxed black crosses show the centroid of the GC3Ai segmented signal shown in B. **D:** Illustration of the error margin of the compartment boundaries used to account for uncertainty in signal localisation and landmark position. For each compartment, the margin was extended by 11.8 μm in order to encompass surrounding regions. In this example, the compartment defined by landmarks 32;34;43;42 (coloured pink) has its margin extended and as a result the three GC3Ai centroids located around the compartment (boxed black crosses) will be considered as being also part of this compartment. **E-G':** Co-localisation of GC3Ai (green), TUNEL (magenta) and cleaved DCP-1 (*Drosophila* caspase3, red). E-cad in grey. Close-up view of the white dotted square are shown in **E'-G'**. **H-K:** Superimposition of cleaved DCP-1 (**H**, magenta) and TUNEL (**J**, magenta) signals from 35 *w118* discs superimposed using the General Procrustes Alignment (GPA) based on the 36 landmarks positions. Heat-maps showing the average cleaved DCP-1 and TUNEL positive area for each of the 40 compartments are shown in **I** and **K** respectively. Numbers within each compartment show the average value also shown as a colour coded heat-map. **L-Q:** Pattern of GC3Ai in *UAS-Dronc^{DN}* background (**L-N**) and *hid RNAi* background (**O-Q**) driven by GMR11F02-GAL4, single representative wing disc (**L, O** DSRF green, GC3Ai magenta), superimposition of 26 *Dronc^{DN}* discs (**M**) and 25 *hid*-RNAi disc (**P**) using GPA, and heat maps showing the averaged GC3Ai positive area for each genotype(**N,Q**). Note that contrary to the maps shown in **Figure 1 H,I**, the colour-scale is adapted for each genotype to better show spatial differences. **R:** Superimposition of TUNEL positive particles from 31 wing discs homozygous mutant for Dark (*dark$^{[CD4]}$*, *Drosophila Apaf1).* **R':** Heat map showing the averaged TUNEL area for the 31 *dark$^{[CD4]}$* discs. The scale is the same as the map shown in **Figure 1suppK** for TUNEL area in *w118* background, which is the corresponding control. **S,T:** Mean GC3Ai positive area for three genotypes (**S**, *Control*, *hid-RNAi*, *Dronc^{DN}*) and TUNEL positive area in two genotypes (**T**, *dark$^{[CD4]}$, white=w118*) for the 40 compartments. The top-right inset in **S** shows a wing disc diagram with the 40 compartments. Error bars show s.e.m.. All scale bars are 50 μm length excepted in **E'-G'**, 10 μm.

Figure 2

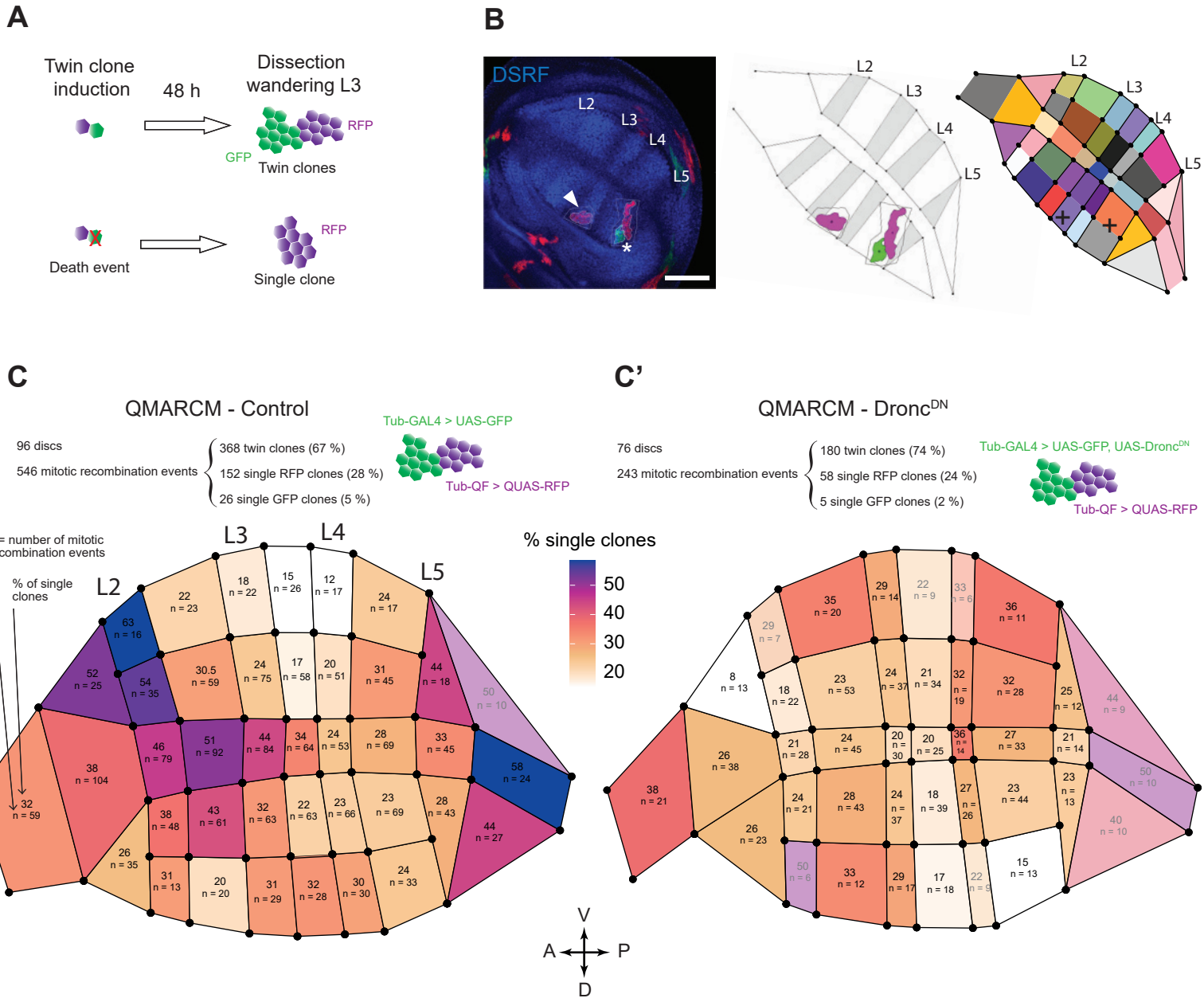
A
Twin clone induction
48 h
Dissection wandering L3
RFP
GFP
Twin clones
Death event
RFP
Single clone
B
DSRF
L2
L3
L4
L5
C
QMARCM - Control
96 discs
546 mitotic recombination events
368 twin clones (67 %)
152 single RFP clones (28 %)
26 single GFP clones (5 %)
Tub-GAL4 > UAS-GFP
Tub-QF > QUAS-RFP
n = number of mitotic recombination events
% of single clones
% single clones
50
40
30
20
C'
QMARCM - Dronc^DN
76 discs
243 mitotic recombination events
180 twin clones (74 %)
58 single RFP clones (24 %)
5 single GFP clones (2 %)
Tub-GAL4 > UAS-GFP, UAS-Dronc^DN
Tub-QF > QUAS-RFP
V
A
P
D
D
H99 - FRT80/ arm-lacZ FRT80
66 discs
1242 mitotic recombination events
1140 twin clones (91.8 %)
102 single H99/H99 clones (8.2 %)
0 single +/+ clones (0 %)
+ / +
H99 / H99
H99 / +
β-gal
H99 and WT twin clones
% single clones
30
25
20
15
10
5

Figure 2: clone disappearance is spatially patterned in the developing wing.

A: Rationale for inferring cell death events from twin-clone induction experiments. Upon twin-clone induction and 48 h of growth, the observation of twin clones composed of one GFP and one RFP clone is expected. However, the occurrence of a cell death event soon after clone induction will result in the occurrence of a single GFP or RFP clone without any twin counterpart in its vicinity. **B:** Spatial mapping for twin and single clone occurrences in the wing disc. Left, image of a wing disc at 96 h AEL stained with anti-DSRF and showing a single RFP clone (arrowhead) and a twin clone GFP-RFP (asterisk). Middle, manual segmentation of the tissue using the DSRF signal, and automated segmentation of the clones. Spatial map of the wing disc divided in 40 compartments (following the DSRF-based segmentation) into which clones positions are mapped. **C-D:** Spatial maps showing the pattern of single clone occurrences under different genetic conditions. In each case, the genotypes of the clones, the number of discs studied, the total number of mitotic recombination events, of twin clones, and of single clones observed are given. Colour scale of the heat maps shows the % of single clones observed in each compartment, as a proportion of the total number of mitotic recombination events assigned to this compartment (n). For clarity, the compartments for which n < 10 were shaded, since the inferred proportion from such low sample size are very unreliable. A: Anterior, P: Posterior, V: Ventral, D: Dorsal. **C-C':** Spatial map of single clone occurrences obtained by inducing twin clones using the twin spot QMARCM system, in control conditions (**C**) and by additionally expressing UAS-Dronc^{DN} in the GFP clone (**C'**). **C** and **C'** share the same colour scale. **D:** Spatial map of single clone occurrences (% for each compartment) obtained by inducing twin clones using mitotic recombination and the H99 deletion (covering the pro-apoptotic genes *hid*, *grim* and *reaper*) with *arm-LacZ* allele to mark the sister WT chromosome, left scheme shows the β-gal signal associated with each genotype (dark: homozygous mutant, 2 β-gal copies: WT, 1 copy: heterozygous). A representative wing disc is shown on the bottom left (green: β-gal). White stars show twin clones, dotted square and close up view an example of single *H99* mutant clone. Scale bar=50μm.

Supplementary figure 2

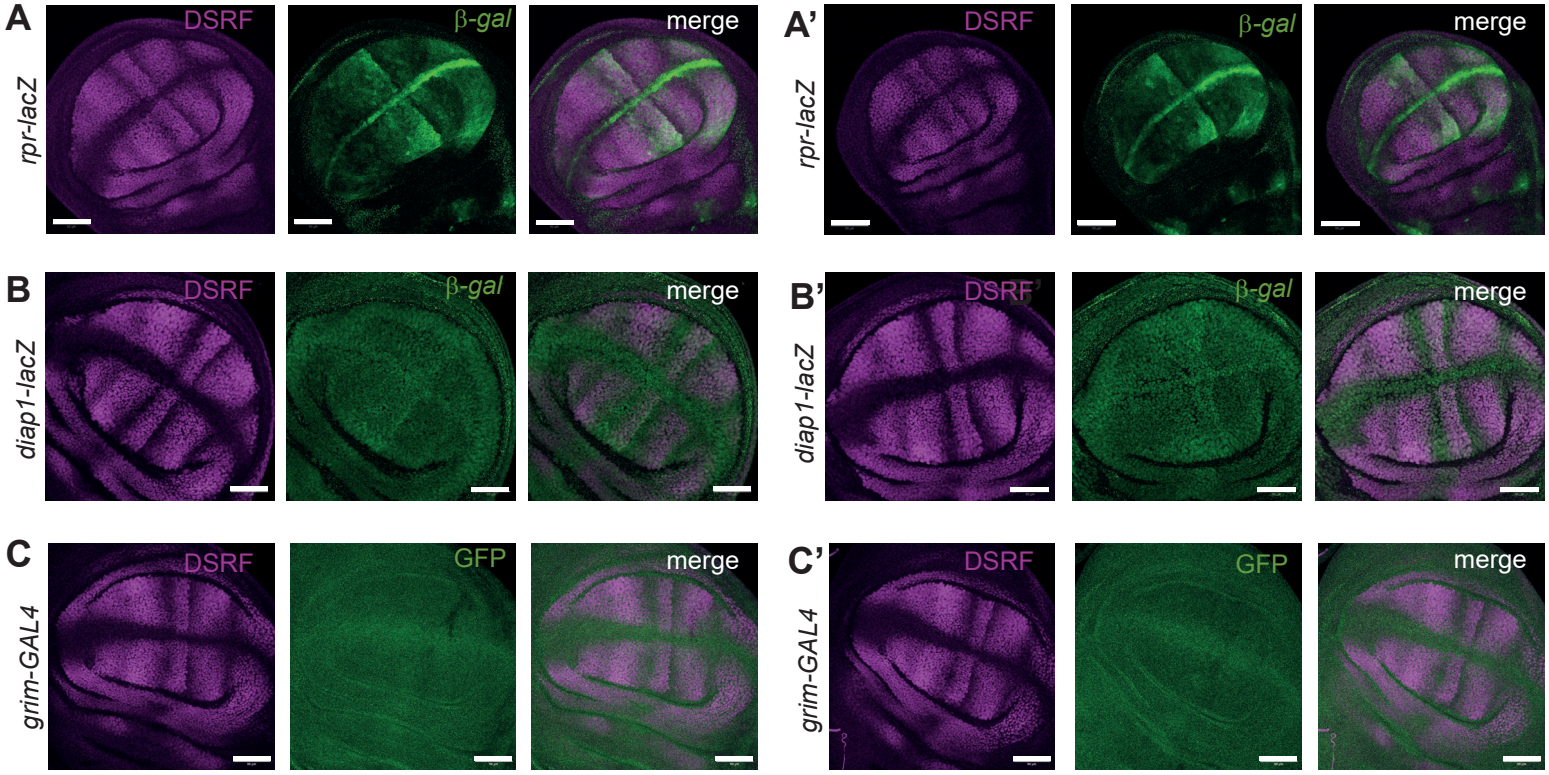

D

$$\text{Ratio} = \frac{(\text{area GFP clone}) - (\text{area RFP clone})}{(\text{area GFP clone}) + (\text{area RFP clone})}$$

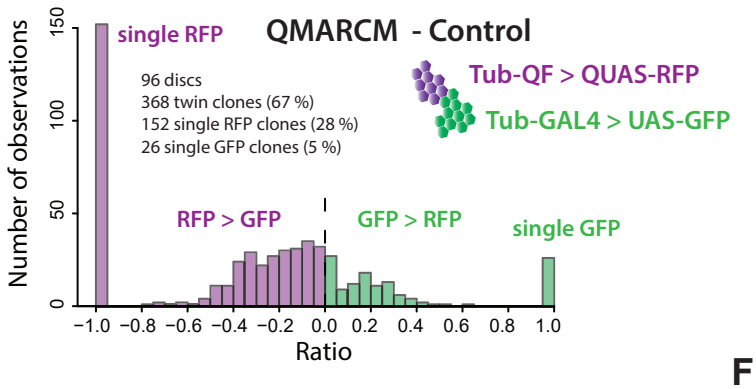

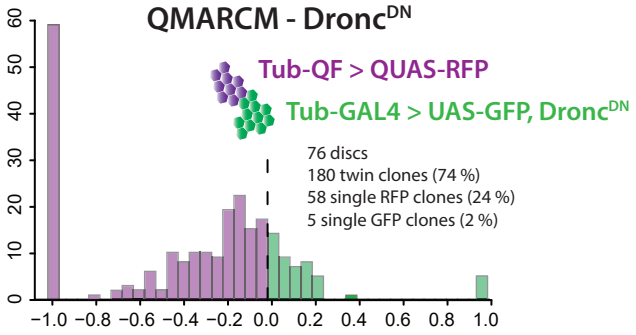

E

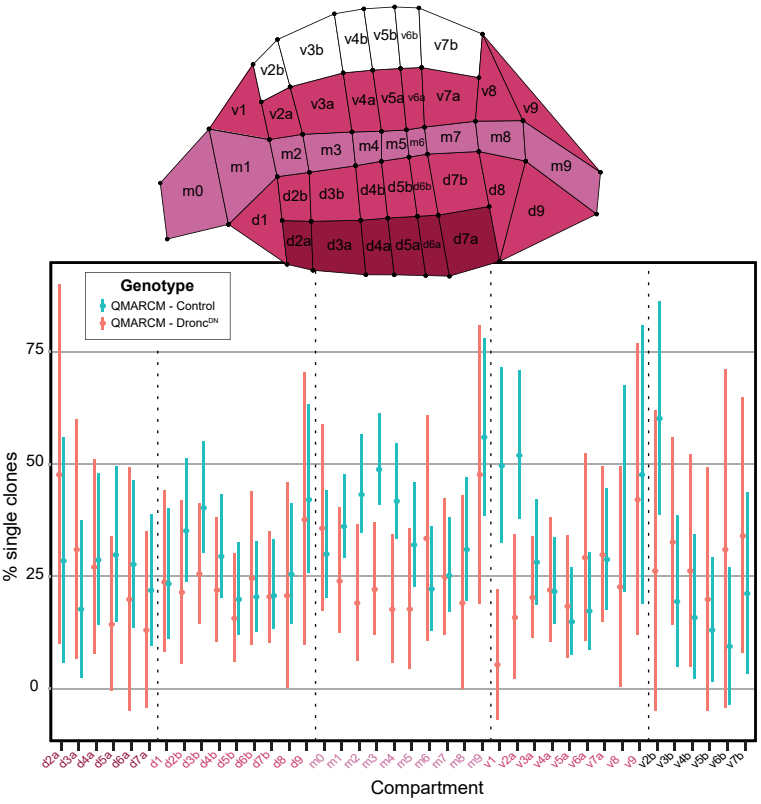

F

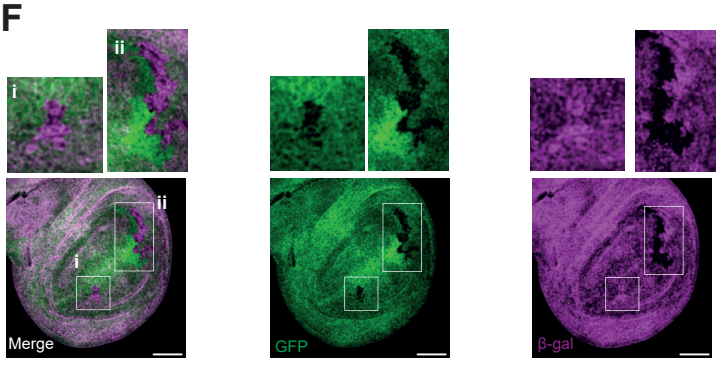

G

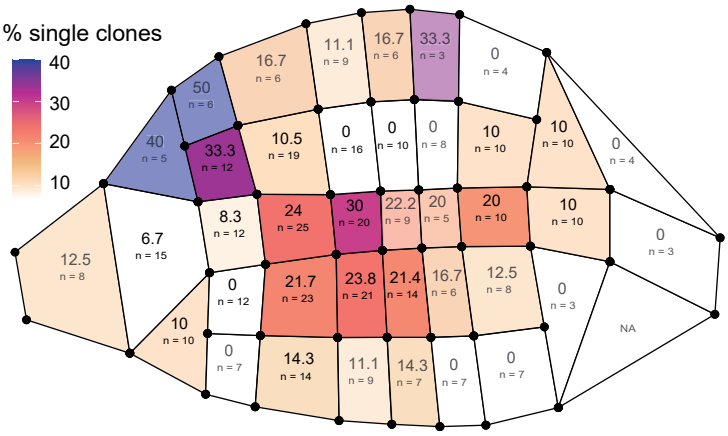

Supplementary figure 2 (related to Figure 2)

A, A': z-projection of two wing discs expressing *rpr-LacZ* reporter (green, β-gal staining) and stained with DSRF (magenta). **B, B':** z-projection of two wing discs expressing *diap1-LacZ* reporter (green, β-gal staining) and stained with DSRF (magenta). **C, C':** z-projection of two wing discs expressing *grim-GAL4 UAS-GFP* reporter (green, GFP signal) and stained with DSRF (magenta). Scale bars from **A** to **C'**=50μm. **D:** Distribution of twin-clone Ratio values for each of the two genetic conditions studied to establish the spatial map of single clone occurrences with QMARCM. For each mitotic recombination event, the computed ratio is the difference between areas of the green and red clones over the sum of these areas. Negative ratios indicate twin clones for which the red clone is bigger than the green one whereas twin clones where the green clone is bigger than the red one have positive values. Ratios values of -1 and +1 indicate mitotic recombination events where the green or the red clone were lost and have thus a null area. **E:** Frequency of the single colour clones for the 40 compartments in four genotypes (QMARCM blue, QMARCM Dronc^{DN} red). A wing disc diagram shows the delimitation and names of the 40 compartments on which the quantifications were made. Error bars are s.e.m. **F:** Example of a wing disc obtained by inducing twin clones using mitotic recombination between nls-GFP and arm-β-gal, stained for anti β-gal. A single plane is shown, processed with a gaussian blur filter 3D (x = 2, y = 2, z = 1) and illustrating an example of a single clone β-gal 2x (inset i) and of a twin clone β-gal 2x/GFP 2x (inset ii). Scale bars: 50 µm. **G:** Spatial map of single clone occurrences (% for each compartment) obtained by inducing twin clones using mitotic recombination between nls-GFP and arm-β-gal. Colour scale shows the % of single clones observed in each compartment, as a proportion of the total number of mitotic recombination events assigned to this compartment (n).

Figure 3

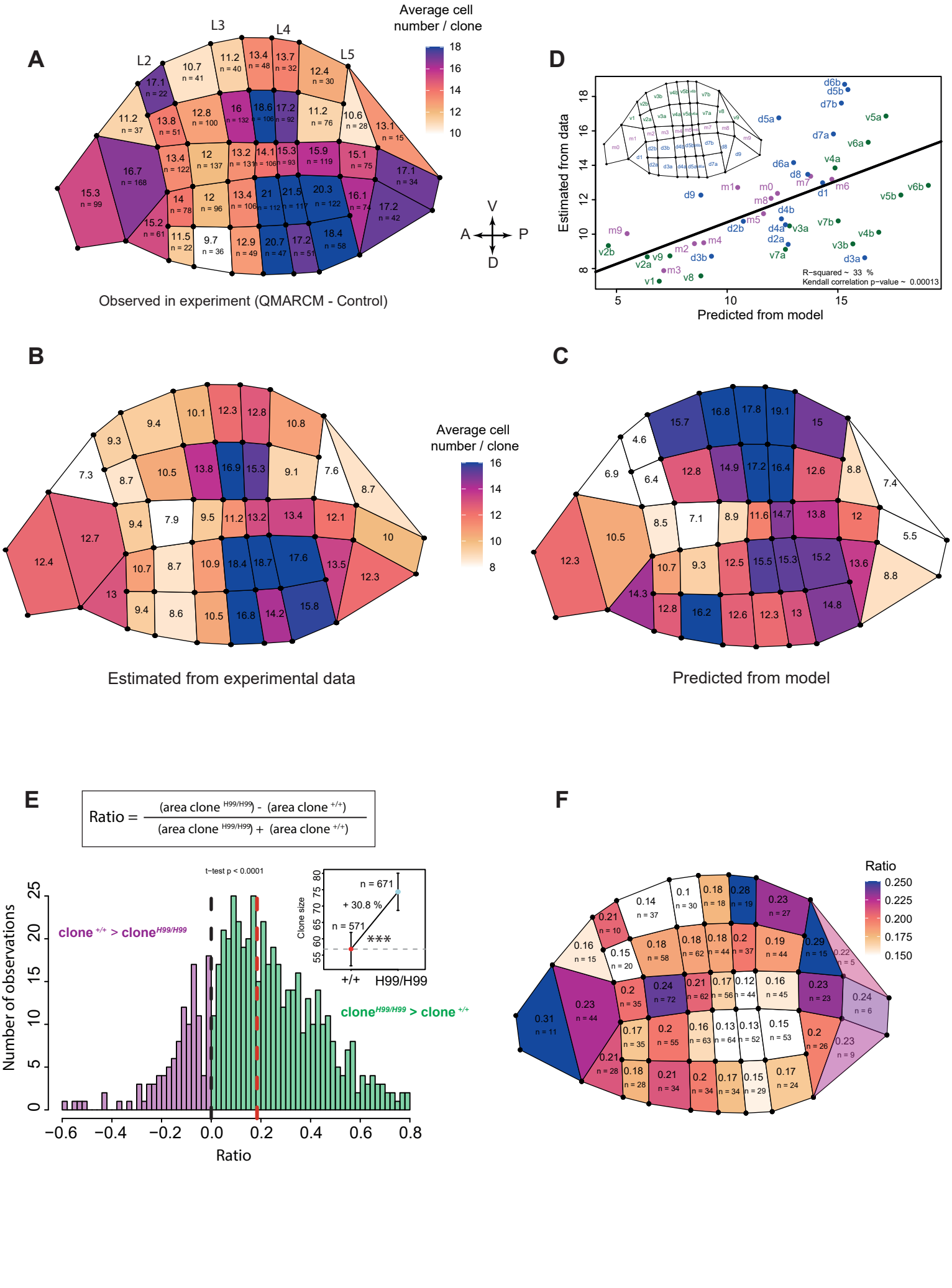
A
L2
L3
L4
L5
Average cell number / clone
18
16
14
12
10
V
A
P
D
Observed in experiment (QMARCM - Control)
D
Estimated from data
Predicted from model
R−squared ~ 33 %
Kendall correlation p−value ~ 0.00013
B
Average cell number / clone
16
14
12
10
8
Estimated from experimental data
C
Predicted from model
E
Ratio = (area clone H99/H99) - (area clone +/+) / (area clone H99/H99) + (area clone +/+)
t−test p < 0.0001
clone +/+ > clone H99/H99
clone H99/H99 > clone +/+
Number of observations
Ratio
Clone size
n = 671
+ 30.8 %
n = 571
***
+/+
H99/H99
F
Ratio
0.250
0.225
0.200
0.175
0.150

Figure 3: Spatial variation of apoptosis modulates local growth and clone size

A: Spatial map for average cell number per clone in QMARCM – control experiment. Clones were considered irrespective of their colour. For each compartment, the average clone surface was calculated and divided a posteriori by the average cell apical size obtained in the same compartment to obtain an estimation of the averaged cell number per clone (see **Methods** and **Figure 3supp**). **B:** Spatial map of the mean value of clone size ($\mu(t)$, see **Methods**) which integrates the experimental average clone size as well as the 0 values (estimated from the proportion of singe colour clone, see **Methods**). **C**: Spatial map of the averaged predicted number of cells per clone assuming a constant and homogenous growth rate throughout the pouch and heterogeneous rate of apoptosis estimated from the local proportion of single coloured clone (see **Methods**). **B** and **C** share the same colour scale bar. **D:** Correlation between the average cell number per clone predicted from the model and estimated from experimental data for each compartment. The black line is the linear regression. The R-squared of the regression and the p-value of a correlation test (Kendall) are shown. Each dot is the data for one compartment, coloured and named according to the map shown on the left side of the plot (blue: dorsal compartments d1 to d9; magenta: margin compartments m0 to m9; green: ventral compartments v1 to v9). **E:** Distribution of twin-clone area ratio values for each H99 mitotic clones (H99 homozygous mutant versus WT sibling clone). For each mitotic recombination event, the computed ratio is the difference between areas of the H99 and WT clones over the sum of these areas (top inset). Negative ratios: WT clone bigger than H99 clone, Positive ratios: H99 clone bigger than WT clone. Black dotted line shows 0, red dotted line the median of the distribution. Top right inset shows the bulk averaged clone size (30.8% bigger for H99 compared to WT, $p<0.0001$), dots averages, error bars 95% confidence intervals, n, number of clones. Note that single clones were not used for this comparison (which would have a value of +1 or -1). **F:** Spatial map for averaged clone size ratio for H99 and WT sibling clones (see in **E**) for each of the 40 compartments of 66 wing discs. Colour scale is shown on the right.

Supplementary figure 3

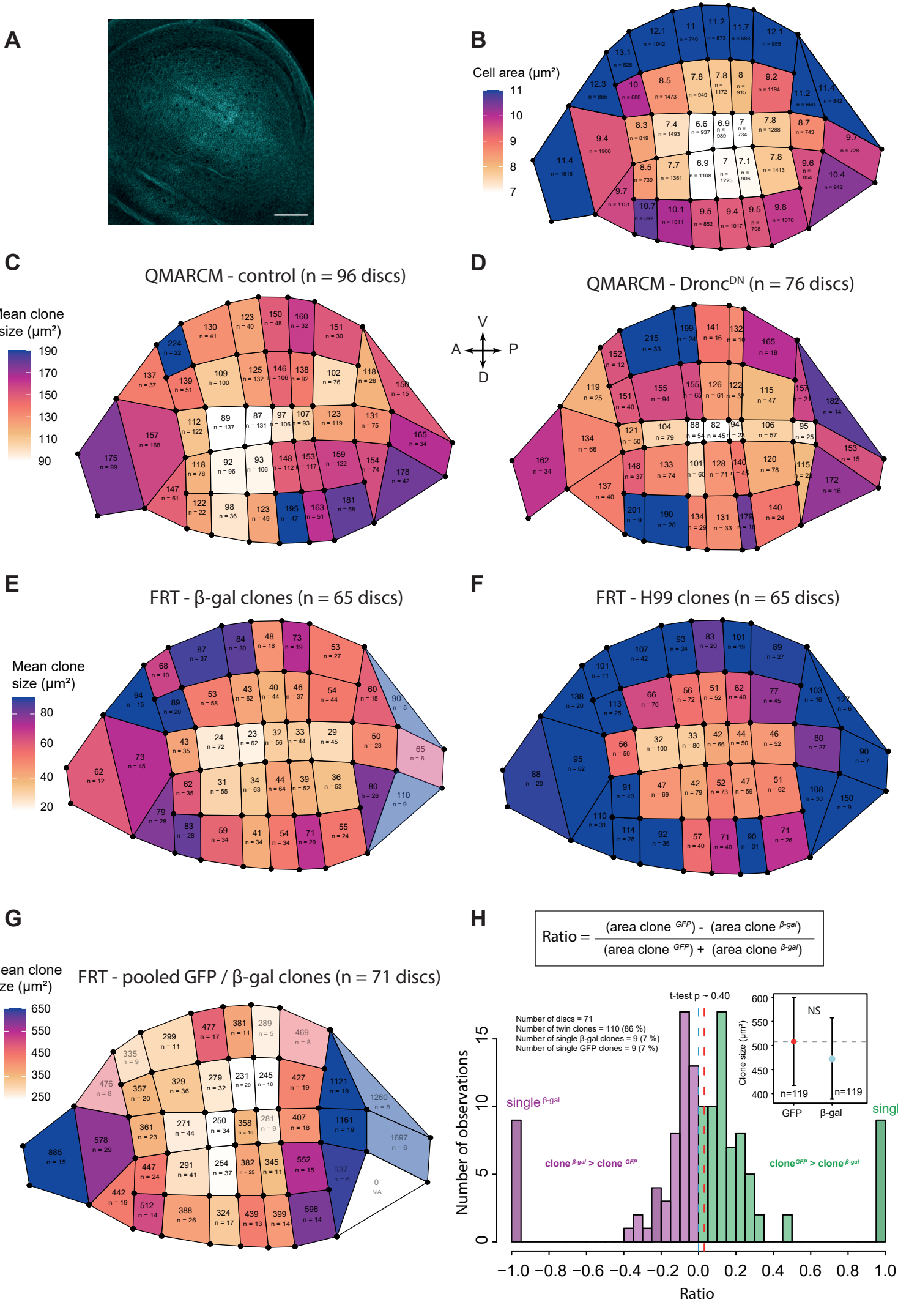

Supplementary figure 3 (associated with Figure 3)

A: Example of a local projection of a wing disc stained with E-cad used for cell apical area measurments. Scale bar=50 µm. **B:** Heat map showing the average spatial pattern for cell apical area from three discs . Within each compartment, the value for average cell size (µm²) and the number of cells measured (over the three discs) are given. Overall, the three discs had very similar patterns of spatial variation of cell apical area (not shown). **C-G:** Heat maps showing the average spatial pattern for clone surface area (µm²). For each compartment, the average surface area of the clones and the number of clones examined (n) are given. The data are shown for five conditions: QMARCM system, in control conditions (tub-QF, QUAS-RFP and tub-Gal4, UAS-GFP) (**C**) and upon expression of UAS-Dronc^{DN} in the GFP clone (**D**); twin FRT clones H99/ β-gal for β-gal clones (**E**) and H99 homozygous clones (**F**); neutral twin FRT clones GFPnls/β-gal for GFP and β-gal clones pooled together (**G**) Note that the colour scale is different between **C,D** ; **E,F** ; and **G**. Compartments for lower sample sizes (n < 10) are shaded. Note that colour scales of heat maps were saturated to better display relevant local variations. **H:** Distribution of twin-clone area ratio values for neutral FRT GFPnls/β-gal mitotic clones (homozygous GFP versus homozygous β-gal sibling clone). For each mitotic recombination event, the computed ratio is the difference between areas of the GFP and β-gal clones over the sum of these areas (top inset). Negative ratios: β-gal clone bigger than GFP clone. Positive ratios: β-gal clone smaller than GFP clone. Blue dotted line shows 0, red dotted line the median of the distribution (not different from zero, t-test p-value ~ 0.40). Top right inset shows the bulk averaged clone size (no difference between GFP and β-gal t-test p-value ~0.58), dots averages, error bars 95% confidence intervals, n, number of clones. Note that values of +1 and -1 denote the presence of single clones (single GFP and single β-gal respectively).

Figure 4

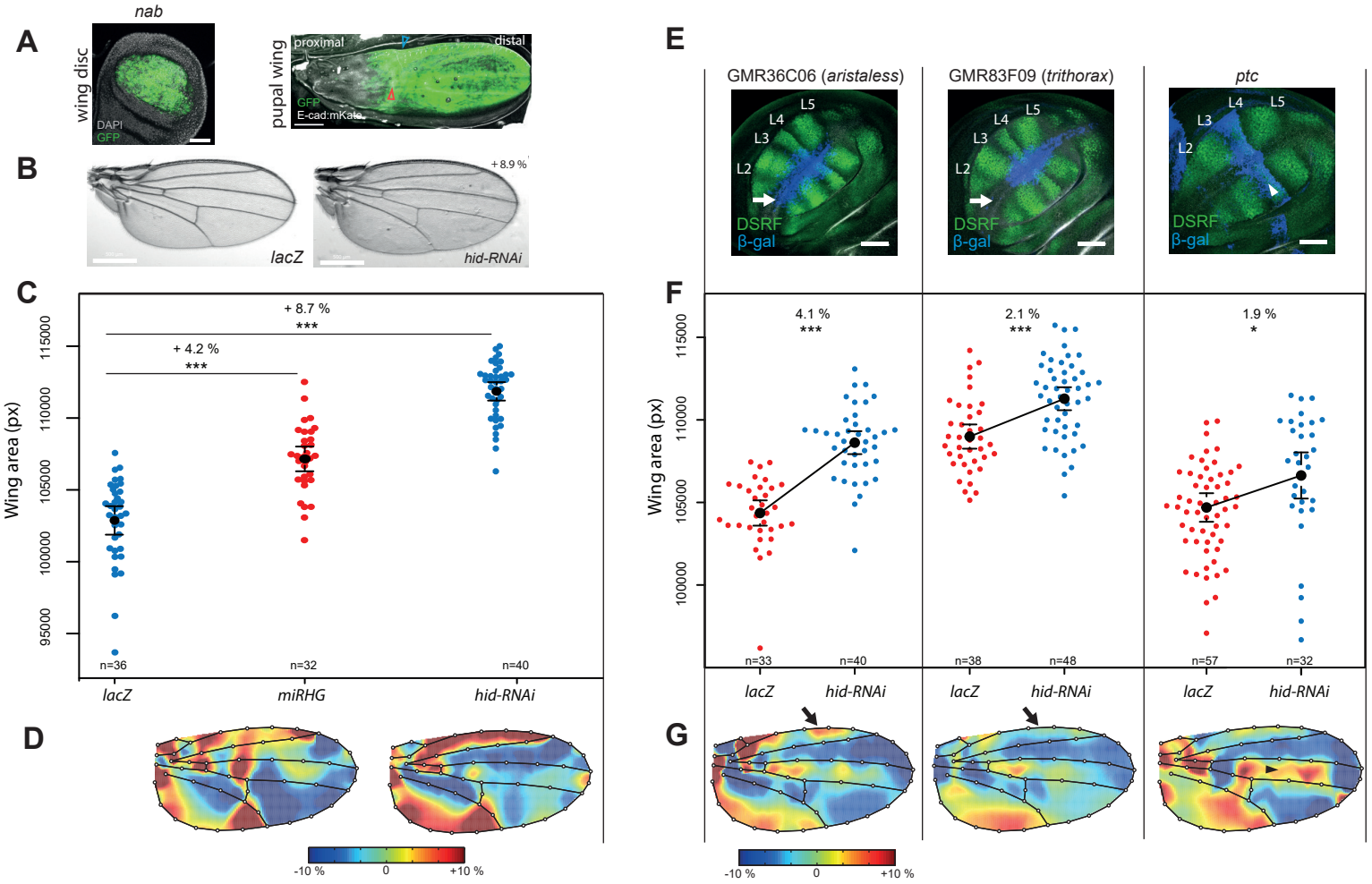
A
nab
wing disc
DAPI
GFP
pupal wing
proximal
distal
GFP
E-cad:mKate
B
+ 8.9 %
lacZ
hid-RNAi
C
+ 8.7 %
***
+ 4.2 %
***
Wing area (px)
95000
100000
105000
110000
115000
n=36
n=32
n=40
lacZ
miRHG
hid-RNAi
D
-10 %
0
+10 %
E
GMR36C06 (aristaless)
GMR83F09 (trithorax)
ptc
L2
L3
L4
L5
DSRF
β-gal
F
4.1 %
***
2.1 %
***
1.9 %
*
Wing area (px)
100000
105000
110000
115000
n=33
n=40
n=38
n=48
n=57
n=32
lacZ
hid-RNAi
G
-10 %
0
+10 %

Figure 4: Apoptosis affects locally and globally wing size and shape.

A: Pattern of expression at ~ 96 h AEL of the Nab-GAL4 driver used to express *hid-RNAi* at larval stage (left, GFP, green) and pupal stage (right, 30h APF, GFP, green, E-cad::mKate, magenta, red and blue arrowhead point at the hinge/blade boundary recognised by the accumulation of E-cad along antero-posterior axis (red arrowhead) and the infold on the anterior side (blue arrohead). Scale bars, 50μm top, 200 μm bottom. **B**: Images of adult wings in the control (*Nab-GAL4, UAS-LacZ, Area=103661 px*) and upon downregulation of apoptosis by *hid* depletion (*Nab-GAL4, hid-RNAi, Area =112857px*). Wings are bigger and slightly rounder. The images shown are representative of the average size observed in control and *hid* downregulation groups and differ by 8.9 % in area. Scale bars, 500 μm. **C:** Variation of adult wing size in control (*UAS-LacZ*), upon expression of the microRNA targeting *hid, grim* and *reaper* (*miRHG*) and depletion of Hid (*hid-RNAi*) all with the Nab-GAL4 driver. Each dot is a wing. Black dots are means and error bars 95% confidence interval. n=number of wings. ***: $p < 0.0001$. **D:** Local variation of tissue shape caused by expressing *miRHG* or *hid-RNAi* relative to the control wing (*lacZ*). Colours represent changes in relative area necessary to transform the average wing from the control group to the perturbed group after alignment, rotation and size normalisation, red expansion, blue shrinkage (number of wings shown in **C**). Note that this comparison is done after rescaling the wings in order to compare variations of shape. Colour bar shows the upper and lower limits in deformation. Highest colour intensity is reached at 10% increase and decrease in local area. Left: proximal, right: distal, top: anterior, bottom: posterior. **E:** Pattern of expression in the wing disc at ~ 96 h AEL of various GAL4 drivers used to express *hid-RNAi*. Green, DSRF, blue, UAS-β–gal. L2,L3,L4,L5 show the different prospective veins. White arrows show the most anterior region of the disc, where GAL4 is expressed in the case of *aristaless-GAL4*, but not in the case of *trithorax*-GAL4. Scale bars, 50μm. Left: anterior, right: posterior, top: ventral, bottom: dorsal. **F:** Variation of adult wing size for the different genotypes. Each dot is a wing. Black dots are means and error bars 95% confidence interval. n=number of wings. ***: $p < 0.0001$, *: $p = 0.02$. **G:** Local variations of tissue shape caused by expressing *hid-RNAi* relative to the control wing (*lacZ*) for each GAL4 driver. Colours represent changes in relative area necessary to transform the average wing from the control group to the perturbed group, red expansion, blue shrinkage (number of wings shown in **F**). Left: proximal, right: distal, top: anterior, bottom: posterior.

Supplementary figure 4

A

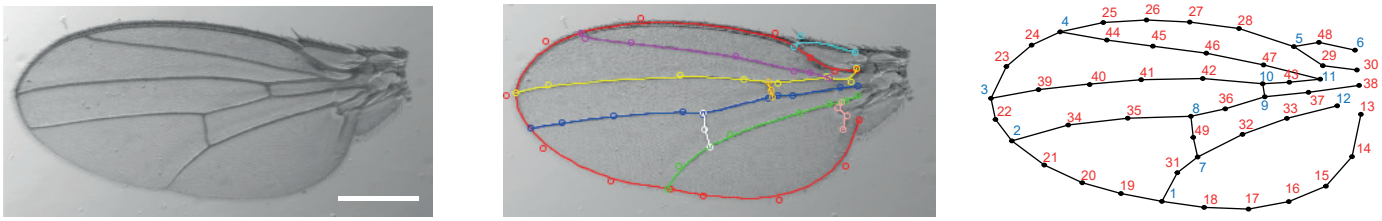

B

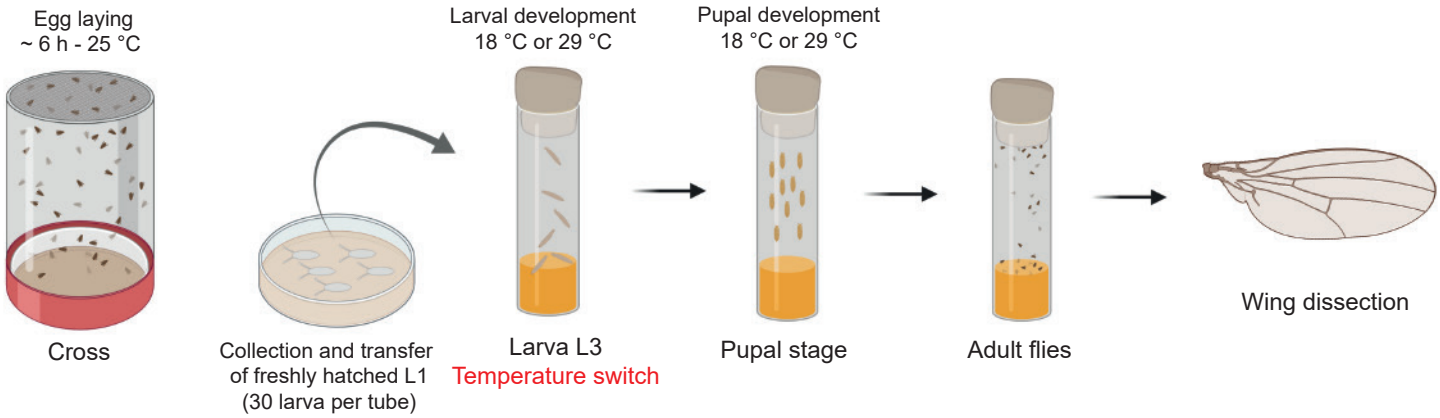

C

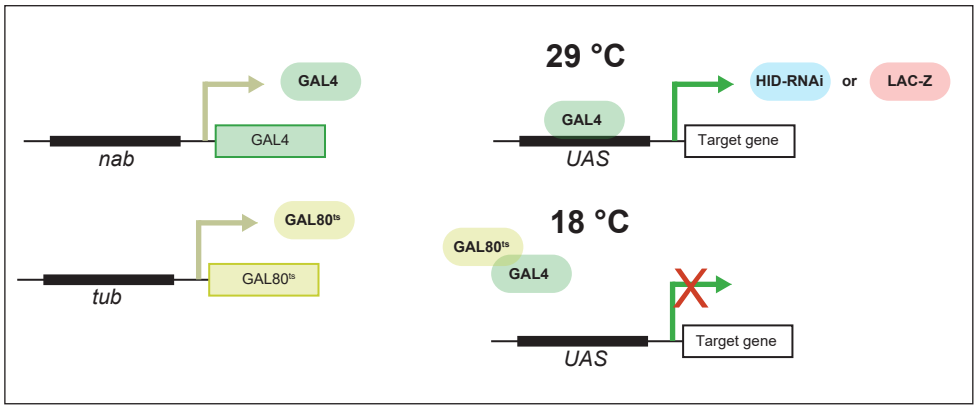

4 conditions

Condition	Larva	Pupa
No expression	18 °C	18 °C
Larval expression	29 °C	18 °C
Pupal expression	18 °C	29 °C
Larval + Pupal expression	29 °C	29 °C

Supplementary figure 4 (related to Figure 4 and Figure 5)

A: Adult wing segmentation pipeline. Left: wing example. Middle: the software Wings4 fits 9 spline curves (i.e., equations that give the location of the curve at any point between its end points) to veins and edges of the wing. Each spline is shown with a specific colour. Circles denote the positions of control points, which can be dragged manually by the user to maximise the overlap between the spline curves and veins and edges of the wing. Left: the program CPR extracts from the spline curves the positions of 12 landmarks (blue, numbered 1-12) and 36 semi-landmarks (red, numbered 13-48). Landmarks are strongly reliable points because they are located at the end of the curves. Semi-landmarks are less reliable because they are sampled along the curves by spacing them equally along each curve segment between each pair of landmarks. **B:** Experimental design for conditional gene expression during early or late developmental stages. Flies were crossed in cages supplied with agar petri dishes and allowed to lay eggs for ~ 6 h. Freshly hatched larva were transferred to regular vials at a density of 30 individuals / tube, and placed at 18 °C or 29 °C. Once arrived at the L3 wandering stage, individuals were switched temperature (from 18 °C to 29 °C and vice-versa). Upon hatching flies were collected for wing dissection. **C:** Rationale for conditional gene expression using tub-GAL80ts. GAL80ts has ubiquitous expression under the control of tubulin promoter whereas GAL4 expression is restricted to wing tissue under the control of GMR11F02-GAL4. At 18 °C, GAL80ts binds to the GAL4 and inhibits its activator function, precluding the expression of the target genes. At 29 °C Gal80ts is unable to bind GAL4, allowing GAL4 binding to the upstream activating sequence (UAS) and transcription of target genes (*lacZ* or *hid-RNAi*).

Figure 5

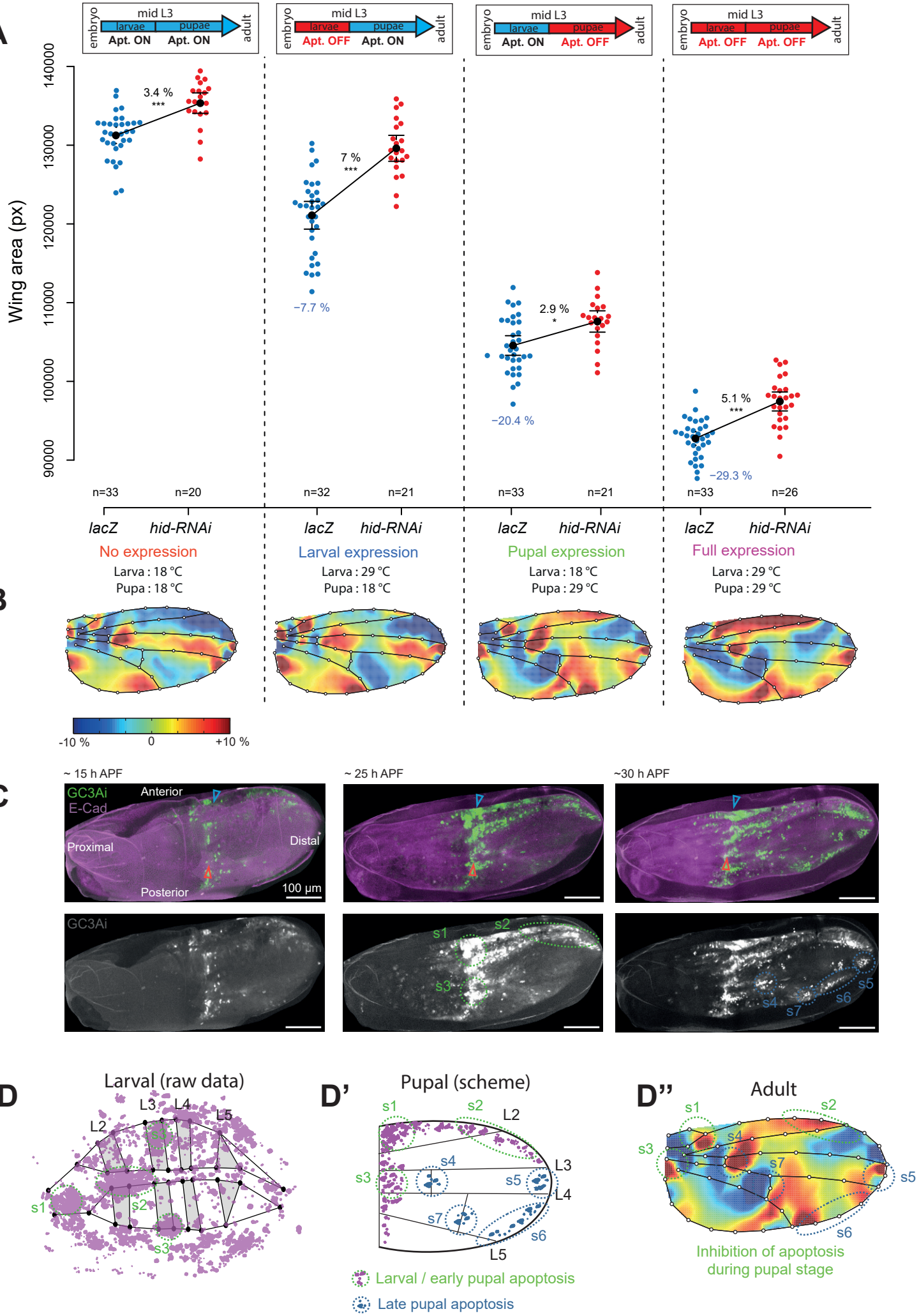
A
embryo
mid L3
larvae
pupae
adult
Apt. ON
Apt. ON
Apt. OFF
Apt. ON
Apt. ON
Apt. OFF
Apt. OFF
Apt. OFF
Wing area (px)
140000
130000
120000
110000
100000
90000
3.4 %
***
7 %
***
−7.7 %
2.9 %
*
−20.4 %
5.1 %
***
−29.3 %
n=33
n=20
n=32
n=21
n=33
n=21
n=33
n=26
lacZ
hid-RNAi
No expression
Larva : 18 °C
Pupa : 18 °C
Larval expression
Larva : 29 °C
Pupa : 18 °C
Pupal expression
Larva : 18 °C
Pupa : 29 °C
Full expression
Larva : 29 °C
Pupa : 29 °C
B
-10 %
0
+10 %
C
~ 15 h APF
~ 25 h APF
~30 h APF
GC3Ai
E-Cad
Anterior
Proximal
Distal
Posterior
100 µm
GC3Ai
s1
s2
s3
s4
s5
s6
s7
D
Larval (raw data)
L2
L3
L4
L5
s1
s2
s3
D'
Pupal (scheme)
L2
L3
L4
L5
Larval / early pupal apoptosis
Late pupal apoptosis
D''
Adult
Inhibition of apoptosis
during pupal stage

Figure 5: Larval and pupal patterned apoptosis affects adult wing size and shape

A: Variation of adult wing size in control (*UAS-LacZ*) and upon depletion of Hid (*hid-RNAi*) with the Nab-GAL4 driver and conditional activation at different developmental stages using the thermosensitive GAL4 inhibitor $GAL80^{TS}$ and controlled temperature shift (29°C, Hid depletion, 18°C no Hid inhibition). See **Figure 4supp**. The % in black show that variation between the Hid RNAi and corresponding control. The % in blue show the variation of size for the control at a given temperature relative to the 18° control (no expression). The top schemes show the period of development during which apoptosis is inhibited. Each dot is a wing. Black dots are means and error bars 95% confidence interval. n=number of wings. ***: $p < 0.0001$, *: $p=0.001$. **B:** Local variation of tissue shape caused by expressing *hid-RNAi* relative to the control wing (*lacZ*) for each temperature condition. Colours represent changes in relative area necessary to transform the average wing from the control group to the perturbed group, red expansion, blue shrinkage (number of wings shown in **A**). Highest colour intensity is reached at 10 % increase and decrease in local area. Left: proximal, right: distal, top: anterior, bottom: posterior. **C:** Snapshots of z-local projections of a live pupal wing expressing UAS-GC3Ai (green) in the Nab-GAL4 domain (wing pouch) and E-cad::mKate between 16 and 32h APF (hours After Pupal Formation). See **Video S1**. Representative of 4 movies. s1 to s3 and green ellipses show early domains of apoptosis (already appearing at 16h APF), s4 to s7 and blue ellipses show late domains of apoptosis (appearing around 30h APF). Blue and red arrowheads show the position of the margin between the blade and hinge, marked with a infold on the anterior side (blue arrowhead) and strong concentration of E-cad along AP axis (red arrowhead). Scale bars=100μm. **D:** Averaged pattern of apoptosis in the wing disc (**Figure 1F**) and the corresponding early pupal apoptosis zones (s1 to s3, green ellipses). Anterior: left, posterior: right, ventral: top, dorsal: bottom. **D':** Schematic of the apoptosis pattern observed in the pupal wing with early domains (s1 to s3, green ellipses) and late domains (s4 to s7, blue ellipses). Note the correspondence between early domains and the pattern of apoptosis observed in the wing disc (**D** magenta dots). Left: proximal, right: distal, top: anterior, bottom: posterior. **D'':** Map of wing deformation associated with Hid inhibition at pupal stage (**5 B**, pupal expression), red expansion, blue constriction relative to the control discs, and the position of the pupal apoptosis zones (early, s1 to s3, green ellipses, and late, s4 to s7, blue ellipses). Left: proximal, right: distal, top: anterior, bottom: posterior.

Supplementary figure 5

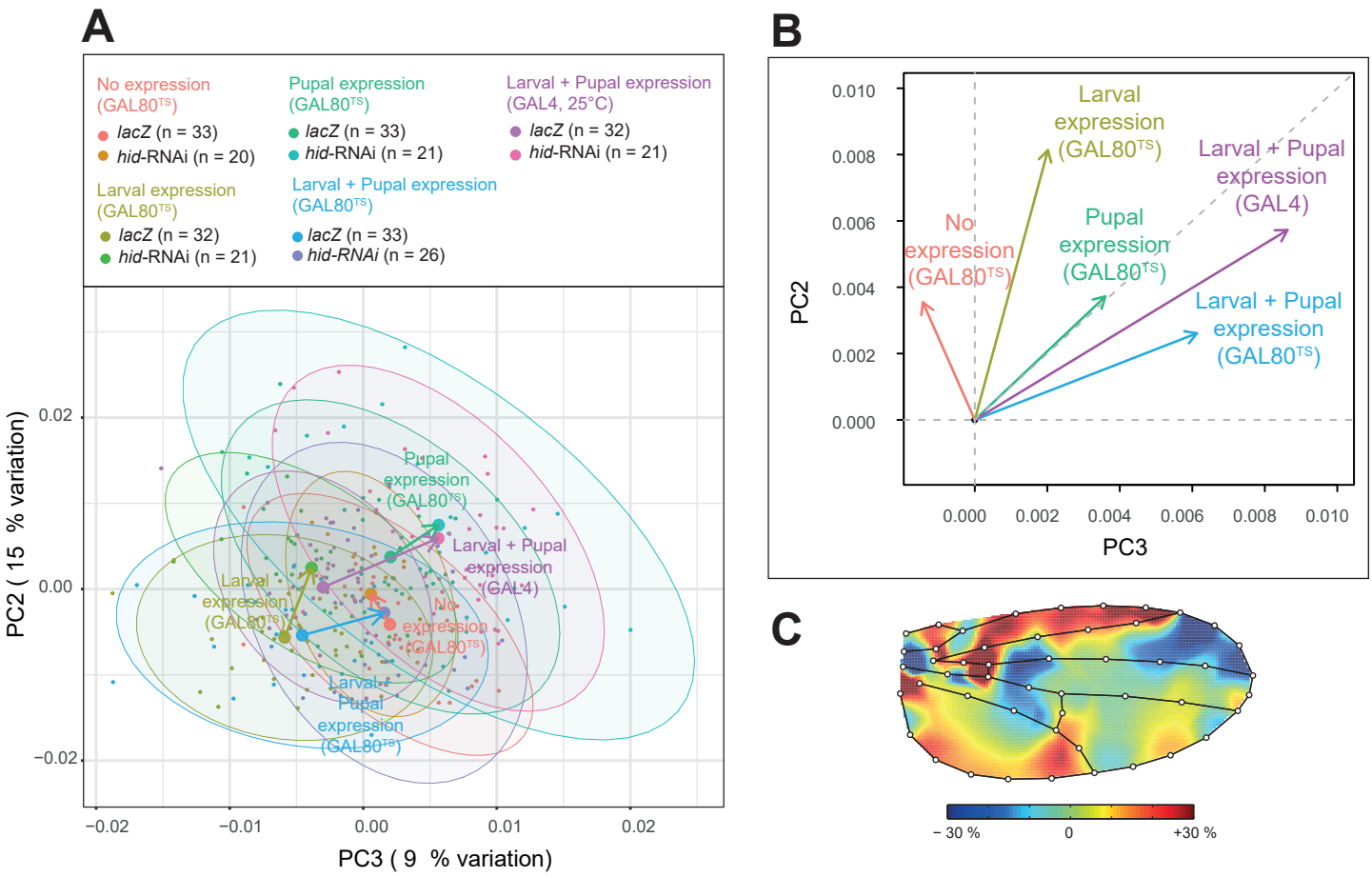

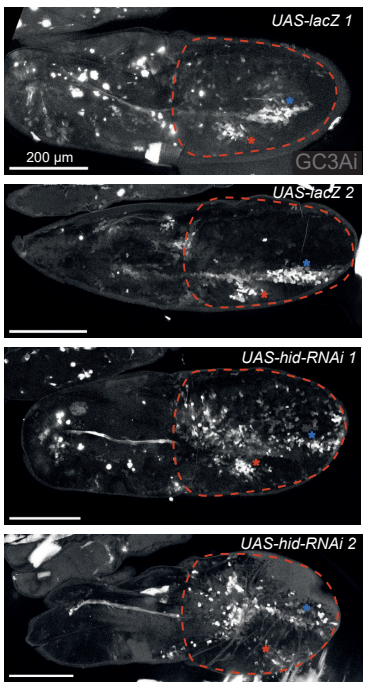

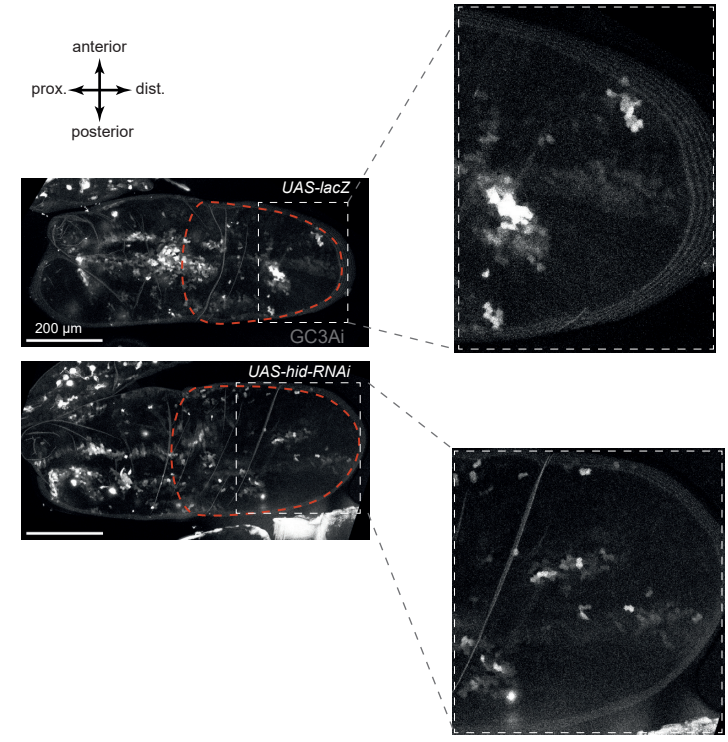

Supplementary figure 5 (related to Figure 5)

A: Principal Component Analysis of adult wing shape using the position of every landmark as inputs (see **Figure 4suppA**) comparing *Nab-GAL4, UAS-LacZ* and *Nab-GAL4, UAS-hid RNAi* with Gal80^{TS} for different temperature switches (see **Figure 5**). The first principal component, which was mostly reflecting the variation driven by the temperature, was removed in order to focus on shape variation associated with the genotypes and *hid* depletion. Each dot represents one wing, the ellipses contain 95% of the data and bold dots are the median of each genotype (number of wings shown in the legend). Vectors represent the transformation in the morpho-space to go from the control to the Hid depleted flies for a given temperature protocol. **B:** The same vectors represented separately. Variations along PC3 (x-axis) reflects the shape variation associated with Hid depletion, which is stronger upon full depletion (all developmental stages). Note that the sum of larval and pupal depletion variations along PC3 axis matches the amplitude of the full depletion along PC3 axis. **C:** Representation of the shape variation along PC3 showing the transformation required to go from the two extreme wings along PC3 (from low to high PC3) after scaling, rotation and translation. Red regions are expanding, blue regions are shrinking (max variations of +/-30%). Overall, movement toward the right on PC3 is associated with a rounding of the wing (expansion of the anterior and posterior sides, shrinkage of the most distal parts). Left: proximal, right: distal, top: anterior, bottom: posterior. **D:** Maximum z-projections of pupal wings expressing *lexAOP-GC3Ai* under the control of *act-lexA*. *UAS-lacZ* or *UAS-hid-RNAi* were conditionally expressed with *tub-GAL80^{TS}* in the *nab-GAL4* domain during the larval stage, by growing the larva at 29 °C and shifting them at 18 °C mid-L3 stage. Acquisitions were done 48 h +/- 6 h after temperature shift. The presumptive blade domain is outlined with a dashed red line. Asterisks mark GC3Ai figures consistently observed in the two controls (*UAS-lacZ 1 and 2*). In *UAS hid-RNAi*, levels of GC3Ai were restored to levels qualitatively similar to the control. **E:** Maximum z-projections of pupal wings expressing *lexAOP-GC3Ai* under the control of *act-lexA*. *UAS-lacZ* or *UAS-hid-RNAi* were conditionally expressed with *tub-GAL80^{TS}* in the *nab-GAL4* domain during the pupal stage, by growing the larva at 18 °C and shifting them at 29 °C at mid-L3 stage. Acquisitions were done 24 h +/- 6 h after temperature shift. The presumptive blade domain is outlined with a dashed red line. The most distal part of the *nab* domain (grey dashed rectangle) is enlarged to appreciate the overall reduction in GC3Ai levels (representative of 3 wings for each).

Supplementary video legends

Video S1: Dynamics of apoptosis in the pupal wing (related to Figure 5)

Local projection of a living pupal wing marked with E-cad::mKate (magenta) and expressing GC3Ai with the Nab-GAL4 driver (green and bottom) between 16h and 35h APF (After Pupal Formation). Anterior: top, Posterior: bottom, Proximal: left, Distal: right. Scale bar=100μm.